EVALUATION OF PITCH CONTROL TECHNIQUES

FOR A CROSS-FLOW WATER TURBINE

by

Timothy Andrew Gauthier

A thesis submitted in partial fulfillment
of the requirements for the degree

of

Master of Science

in

Mechanical Engineering

MONTANA STATE UNIVERSITY
Bozeman, Montana

November 2017

ACKNOWLEDGEMENTS

Countless people have made this work possible. My parents, siblings, and extended family have always been there for me and have cultivated my love for learning. My friends and teachers, from grade school to grad school, and my girlfriend. My advisor Dr. Erick Johnson, who inspired this project and has challenged me to expand the realm of possibility. My committee members Dr. Mark Owkes and Dr. Mike Edens, who have continuously supported me along the way. My friend Pol Llovet, who taught me the ways of high-performance computing. My colleagues in the Fluids and Computations Laboratory, as well as the entire Mechanical Engineering department, who helped to lighten the mood in times of need. Lastly, I am thankful for Cassius, Sheratan, and Ani, and the opportunity to create a better world for them.

TABLE OF CONTENTS

TABLE OF CONTENTS CONTINUED

LIST OF TABLES

Table Page

LIST OF FIGURES

Figure Page

LIST OF FIGURES CONTINUED

Figure Page

LIST OF FIGURES CONTINUED

Figure Page

NOMENCLATURE

θ	azimuthal angle [°]
ω	angular velocity [m/s]
ρ	density [kg/m^3]
λ	tip-speed ratio
$\propto_I$	instantaneous angle of attack [°]
$\propto_n$	nominal angle of attack [°]
Ω	vorticity [s^{-1}]
Ω_{nd}	non-dimensional vorticity
A	turbine swept area [m]
c	chord length [m]
CFD	computational fluid dynamics
CFT	cross-flow turbine
C_p	coefficient of power
$C_{N,T}$	normal/tangential force coefficient
DES	direct-eddy simulation
DS	dynamic stall
$F_{N,T}$	normal/tangential force [N]
HAWT	horizontal-axis wind turbine
HKT	hydrokinetic turbine
k-E	k-epsilon
k-Ω	k-omega
LDV	laser-doppler velocimetry
LEV	leading edge vortex
LES	large-eddy simulation
P	airfoil surface pressure [N/m^2]
P_C	airfoil pressure coefficient
R	turbine radius [m]
RANS	reynolds-averaged Navier-Stokes
RMS	root mean square
SST	shear stress transport
T	turbine torque [N-m]
TEV	trailing edge vortex
U_∞	inflow velocity [m/s]
VAWT	vertical-axis wind turbine

ABSTRACT

Cross-flow water turbines are complex devices that have yet to see large-scale implementation relative to conventional horizontal-axis wind turbines. While wind energy was the primary target of past investigations, water energy follows most of the same dynamic principles. However, water currents tend to be much more stable than their wind current counterparts, and many water currents exist in channels that favor the compact shape of the cross-flow turbine. These advantages have rejuvenated interest in cross-flow turbine design for marine energy generation. Computational models give engineers the ability to accurately estimate what designs work best to avoid costly field maintenance and downtime. Specifically, computational fluid dynamics uses the Navier-Stokes equations, a set of differential equations that describe the pressure and velocity fields in a fluid domain. The Reynold-Averaged Navier-Stokes turbulence model described in this work examines how controlling the pitch of water turbine blades can improve system performance and reliability. Pitch means that the blade noses up or down about the chord line which runs from leading edge to trailing edge relative to the inflow. Pitch control was originally developed for helicopter blades and is commonly used by conventional wind turbines, but pitch control for water turbines is a relatively new research area. Initial results suggest significant incremental gain in power output with pitch control up to 149%, as compared to a no-pitch case, based on a to-scale representation of the cross-flow water turbine in the Fluids and Computations Laboratory at Montana State University. Simultaneous reliability gain is observed as the force transmitted by the water to the blades is reduced by 135%; this may allow for lower cost turbine structures and streamlined hydrofoil design. Additionally, turbine wake profile visualization and blade pressure coefficient curves describe the viscous interaction both quantitatively and qualitatively. Cross-flow water turbines have the potential to become a significant worldwide energy source, with performance optimization studies such as these a necessary prerequisite.

CHAPTER ONE

INTRODUCTION

Hydrokinetic Turbine Technology

While hydrokinetic turbine (HKT) technology in the U.S. is mostly limited to the research and design phase, HKTs exhibit similar characteristics to wind turbines both in terms of device design and grid integration. Moreover, coastal regions with a high population density and limited space for land-based wind turbines may find that ocean and tidal currents (Figure 1) provide a significant medium from which to extract energy (combined potential of 645 TW-hr/year) [1]. Cross-flow water turbines (CFTs) are a type of HKT that bears close resemblance to a vertical-axis wind turbine (VAWT). VAWTs have been studied since the 1970's but have yet to see large-scale implementation in contrast to their horizontal-axis wind turbine (HAWT) counterparts in part due to much more research on the HAWT [2]. Therefore, in order for intelligent HKT selection, the CFT must be better understood for comparison to horizontal-axis.

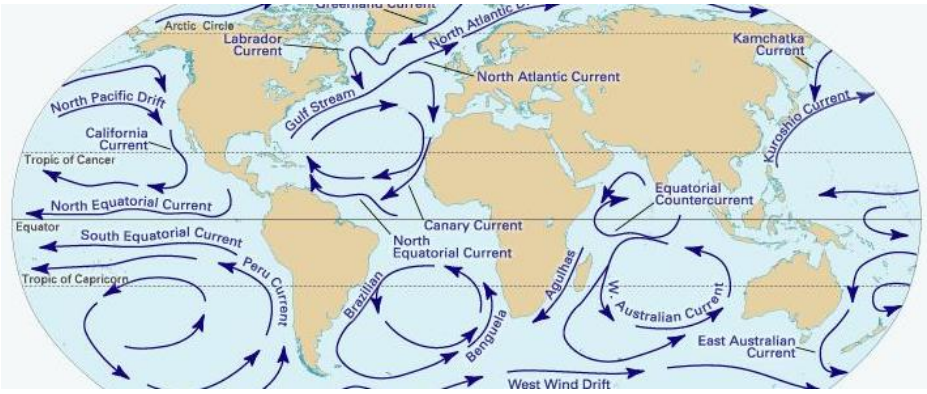

Figure 1: World ocean currents [3]

Performance and Reliability

Since the Industrial Revolutions, humans have constantly looked for better ways to design machines. The vast majority of said designs have been focused on improving machine performance, machine reliability, or both. Performance can generally be thought of as a machine performing its function; just as shovels provide a simple machine (lever) for digging, HKTs convert mechanical energy in the form of spinning to shaft power. Reliability, on the other hand, is the ability of a machine to provide continuous production, which for the HKT implies uninterrupted electricity generation. Conventional electricity generation by harvesting fossil fuels has proven to be extremely reliable; in 2016, NorthWestern Energy of Montana reported 99.98% runtime, which means that power was fully continuous for almost the entire year (save for about 100 minutes) [4]. However, with zero performance, a reliable HKT would be as useful as a rock.

The effect of performance and reliability for any marine hydrokinetic device on cost of energy (COE) is defined simply by Equation 1 [5].

$$COE = \frac{Lifetime\ Energy\ Capture}{Capital\ Cost + Operations\ \&\ Maintenance\ Cost} \quad (1)$$

Lifetime Energy Capture can be attributed directly to how well a device performs; generally, devices that capture more energy will have a higher Capital Cost. Conversely, Operations and Maintenance Cost is driven by reliability of the device. Though performance is typically the primary focus of device design, energy capture can't occur if the device is not operating properly, and the cost associated with excessive maintenance will quickly decrease COE. What this means for the CFT is, both performance and

reliability must be considered to optimize COE. Generally, passive pitch control for the CFT is focused on performance to increase Lifetime Energy Capture. Active pitch control, on the other hand, allows the opportunity to improve reliability based on real-time adjustment to variable and sometimes unpredictable system inputs. In other words, the Operations and Maintenance Cost may be decreased significantly by active control in addition to increased energy capture comparable to that of passive control.

Angle of Attack Control

Some disadvantages of the CFT, which are linked to dynamic stall (DS), include: considerable torque fluctuation and low efficiency relative to horizontal-axis [6]. To decrease fluctuations in torque, pitching of the blades reduces angle of attack primarily to avoid DS. Substantial changes in lift force caused by DS are directly responsible for both likelihood and strength of torque oscillation. Decrease of torque oscillation also increases CFT performance to reduce negative torque. Negative torque means the rotor moves in the opposite direction of power generation; limiting DS can ideally avoid this situation.

Table 1 gives a summary from this work of the possible performance improvement of passive pitch control when compared to a baseline (no-pitch) case varying tip-speed ratio (λ). Tip-speed ratio defines the relationship between input velocity of the water and radial velocity of the turbine blades and ranges anywhere from 1-10 depending on multiple parameters. In order to conduct a manageable study, a range of 1.5-3.0 was chosen because pitch control for a CFT tends to favor lower rotational speeds [6-8]. The results in Table 1 agree with this generalization as $\lambda = 3.0$ has by far the lowest increase due to pitching

(61%). However, the largest increase (249%) occurs not at the lowest speed, but instead at $\lambda = 2.0$. A more detailed analysis can be found in Chapter 4.

Table 1: Coefficient of power per unit span (m^{-1}) by pitching

	$\lambda = 1.5$	**$\lambda = 2.0$**	**$\lambda = 2.5$**	**$\lambda = 3.0$**
Baseline (no-pitch case)	0.0392	0.0525	0.0804	0.1145
Pitching (by harmonic series)	0.1065	0.1831	0.1974	0.1848
Percent increase	171%	249%	145%	61%

CHAPTER TWO

BACKGROUND

State of Hydrokinetic Turbine Research

In its 2017 Annual Energy Outlook, the U.S. Energy Information Administration projects that U.S. renewable energy will increase faster through the year 2050 than all other energy generation by percentage [9]. HKT technology provides a way to generate electricity from water currents, and there is considerable research underway, but no general consensus exists on optimal design type [10-12]. The two most common HKT types are horizontal-axis and vertical-axis (i.e. CFT) [13]. By percentage of HKT systems being studied in 2009, Khan reported 43% of devices as horizontal-axis and 40% as vertical-axis, suggesting a lack of consensus on configuration. Khan also noted that vertical-axis turbines are better suited for use with ducts than horizontal-axis turbines. Ducts are favorable CFTs specifically because they can provide a secondary water current that is environmentally benign. Additionally, ducted CFTs may be favorable for deployment of multi-turbine arrays [14].

Horizontal-Axis vs. Vertical-Axis

For most of the twentieth century, there was little use of electricity generation by wind until around 1973; that year an oil embargo caused a drastic increase in fuel prices throughout the United States [15]. In 1981, a 3 MW Horizontal-Axis Wind Turbine (HAWT) was tested in the United States [15]. The first offshore wind farm was constructed

in 1991, and in 2006, further concerns about the price of oil led to even further development of the HAWT. For wind energy generation, the HAWT is undoubtedly the workhorse in the United States and abroad, and has benefited from many years of engineering optimization.

The Vertical-Axis Wind Turbine, or VAWT, is an energy conversion system traditionally driven by uni-directional wind flow utilizing lift type blades. Its rotational axis is perpendicular to the wind direction and orthogonal to the Horizontal-Axis Wind Turbine, or HAWT. The devices are compared directly in Figure 2; while HAWT blades experience mostly symmetrical flow about their circular swept area, VAWT blades must pass through the wake created by upstream flow on their downstream pass.

Figure 2: Wind turbines compared: a) Darrieus-type VAWT [16], b) HAWT [17]

Vertical-Axis Wind Turbine

Geometry of the VAWT

Figure 3 gives a more detailed look at VAWT dynamics. With the appropriate inflow, blades will turn at a faster rate than the inflow about the turbine rotor. A drivetrain and support structure can be located either above or below the blades; in comparison, HAWT structure are almost exclusively bottom-mounted. With an axis perpendicular to the flow direction, VAWT blades experience variable angle of attack and wake interference throughout each revolution of operation [2]. Both phenomena can increase the likelihood of dynamic stall which, according to Choudhry, decreases life of the blades due to fatigue and increases lift force due to an advanced pitch angle of the blade [18]. However, VAWT design is advantageous in that it does not require a yaw mechanism for inflow changes in direction relative to the HAWT; in other words, a VAWT is "omni-directional".

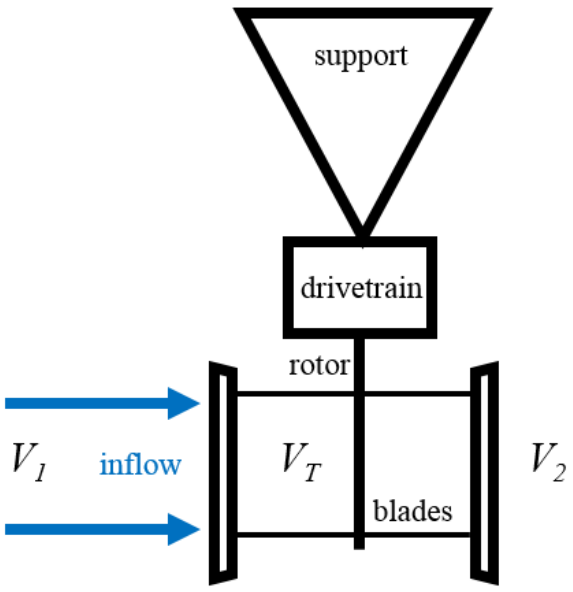

Figure 3: VAWT key components

VAWT Performance

All turbines have a maximum theoretical performance, often referred to as the Betz limit [19]. Though there is some debate as to whether VAWT designs are governed by the same value, velocity at the turbine V_T can be defined as the average of the upstream and downstream velocities, where V_1 is upstream and V_2 downstream as defined in Figure 3. Betz concluded that a maximum output power of 59.3% occurs when V_2 is 1/3 of V_1 [20]. The VAWT also differs from the HAWT in that its area is defined by the cross-sectional area of the turbine. HAWT area equates to that of a circle with its radius being the span of a single blade.

Relevant VAWT Research

Early vertical-axis wind turbine research reached its peak sometime in the nineteen-eighties [21-25], but ultimately the horizontal-axis wind turbine was the preferred system. This shift has been cited as primarily due to the increased complexity of vertical-axis wind turbine movement [2]. However, since about the mid-2000s, there has been a renewed interest in VAWT research.

Migliore conducted one of the earlier studies for VAWTs [23]. He discussed how virtual airfoil aerodynamics and conformal mapping techniques are utilized to convert the curvilinear flow to equivalent rectilinear flow. Strickland took a different approach when he created an aerodynamic vortex model known as VDART (Vortex method of solution for the DARrieus Turbine) for both 2D and 3D analysis [24]. This model was validated with experimental data and is still used to this day for comparison with more advanced techniques. Klimas suggested the use of stream tube models as the simplest approach to

model the blade and wake interaction [21]. Veers is one of the few investigators that considered blade fatigue life as a primary focus, where he proposed a statistical analysis using Rayleigh distributions to describe RMS (root mean square) and binned data [25]. Laneville looked at the dynamic stall phenomenon and the near wake, obtaining the estimated wake location for tip-speed ratios (λs) between one and infinity (with a constant chord/radius ratio of 0.2) [22].

Instead of looking solely at the turbine and its blades for energy conversion, Ferreira analyzed the near wake of the VAWT in order to understand the energy exchange between wake and turbine rotor [2]. Ferreira focuses primarily on the shed vorticity induced by the blade rotation, defined as the rotational wake produced from the trailing edge of the blade in both 2D and 3D flow. To model the system, three methods were used: multiple stream tube, panel/vortex model, and computational fluid dynamics (CFD). Specifically, three different types of CFD were analyzed: Reynolds-Averaged Navier Stokes (RANS), Large-Eddy Simulation (LES), and Detached-Eddy Simulation (DES) which is a hybrid of RANS and LES [2]. The RANS CFD work in this study was validated with Ferreira's data, discussed further in Chapter 3.

Cross-Flow Water Turbine

Studies of the CFT are examined in this section with a particular focus on parameters and characteristics that significantly affect performance and reliability. There may be overlap with VAWT works, but the relative similarity of the CFT (water) vs.

VAWT (wind) makes the titles interchangeable in this context. When in doubt, please refer to the works referenced.

Pros and Cons

The CFT has many advantages in comparison with other turbine designs. CFT design is simple in that the blades are much easier to manufacture than the more intricate HAWT blades. A vertical drivetrain allows for mooring above the water level eliminating the need for an expensive waterproof housing. Decreased noise from CFTs are observed relative to HAWTs in terms of decreased blade tip losses [13]. Khan notes that the orientation of the CFT is also well-suited for skewed flow, mitigating the negative consequence of changing water shear pressure with elevation. In contrast, disadvantages of the CFT include low starting torque, significant torque ripple, and lower efficiency than the HAWT [6]. It is important to note that the higher density and viscosity of water vs. wind means that the CFT will see higher continual loading, but conversely the variability of water current is likely to be much less than that of wind, allowing for more consistent energy capture given a robust design.

Conventional and Unconventional Designs

In 2009, a numerical (CFD) and experimental analysis of a three-bladed CFT was completed [26]. Hwang et al. utilized a 2D RANS k-ω SST turbulence model, where near 50% reduction in tangential force was found from comparing two-dimensional CFD to experimental results. Maitre looked at the influence of three-dimensional operation along with the effect of changing the near wall grid (y^+) value of the CFD model [27]. Maitre's

2D model, also utilizing k-ω SST turbulence, is proportional by a constant of 0.55 to the 3D experiment for tip speed ratios greater than two. These investigations are significant because they provide stipulations for when and how 2D CFD can be applied correctly. A related study was done with the goal to reduce vortex shedding and improve reliability using pitch control [7]. Gorle's turbulence model for these three studies is the 2D RANS k-ω SST model, which combines the near-wall treatment of k-ω with the flow-field realization of k-ε.

Belhache considers radial movement of the blade, i.e. shortening and lengthening of the support arm and turbine radius, to improve CFT performance [28]. Although a novel concept, Belhache does not give a definitive result on if blade performance is improved and leaves ambiguity as to what the key drivers of performance are. Another study, by Zeiner-Gundersen, includes the design and testing of a CFT with flexible foils [29]. Primary benefits of the Zeiner-Gundersen system include a reduction in turbine vibration and a less variable rotational speed with respect to incoming velocity. Also, the Zeiner-Gundersen foil is unique in that it has a rotational pivot point, at about 30% of chord, which allows the blade to pivot to an angle of 7.5 degrees in either direction. Overall, the Zeiner-Gundersen study showed the potential for use of flexible-foils, but did not consider TSR values above 2.2 or compare results to a rigid-foil blade.

Prior Experimental Studies

While a considerable amount of research and design has been performed for the cross-flow water turbine, most studies have been numerical and by their very nature only good for the input parameters they describe. Two experimental cases are described in detail

by Paraschivoui in his book titled *Wind Turbine Design: With Emphasis on Darrieus Concept* [30].

The Texas Tech experiments conducted by Strickland examine a turbine with one to three straight blades of NACA 0012 airfoil type and a chord-to-radius ratio of 0.15 [24]. These studies give considerable information about measurement techniques in terms of wake velocity and blade forces. Wake velocity profiles were obtained from towing a velocity transducer at one- and two-diameters downstream of the turbine rotor. Velocity profiles are but one measure of the energy exchange that takes place within the path of the turbine. Strain gauges are also used on the blade-to-hub linkage to collect normal force and tangential force values. Additionally, a low-pass filter was added to the tangential force measurement to reduce mechanical noise.

Experimenters at the Institut de Mecanique et Statistique de la Turbulence (IMST) experiment was interested in determining the tip-speed ratios at which dynamic stall occurs [30]. Like the Texas Tech turbine, Paraschivoiu notes that the relatively high chord-to-radius ratio in this study (0.3) accentuates dynamic stall effects. Further contributions of the IMST experiment include dye injection from each blade and a good description of how laser-doppler velocimetry (LDV) compares to other wake measurement techniques. Both the IMST and Texas Tech (TXTE) studies are summarized in Table 2.

Table 2: Data from prior experimental studies

	Min λ	*Max* λ	*C/R*	*Airfoil Type*	*# of Blades*
TXTE	2.5	7.5	0.150	NACA 0012	3
IMST	1.0	8.0	0.300	NACA 0018	2

Hydrofoil Effect on Performance

For a CFT to work as intended, selection of the hydrofoil type is important to facilitate lift of the blade which drives turbine movement. Two key parameters are maximum chord thickness and blade camber. A larger chord thickness increases the strength of the blade but a smaller thickness may allow faster movement. Blade camber, according to Ferreira, "significantly affects the loading on the blades, transferring torque between the upwind and downwind blade passages and changing the average normal force." [2].

While airfoils such as the NACA series are well-documented for their use in aerospace and wind energy, usage of airfoils in water energy requires consideration of the differences between wind and water. Water turbine blades, or hydrofoils, operate in a medium which is generally less variable than wind but has a density about 1000 times larger. Previous work by Shiu et al. identified the "MHKF1" brand of cambered hydrofoil; specific to water, the hydrofoils were designed to avoid the adverse effects of cavitation, singing, and the loss of performance when soiled [31]. Cavitation can degrade performance and cause erosion of the foil surface, while singing creates undesirable acoustic noise and mechanical vibration. The MHKF1-180 is chosen for this work, where the number 18 indicates an 18% ratio between maximum chord thickness and chord length. The NACA and MHK airfoil profiles are compared in Figure 4.

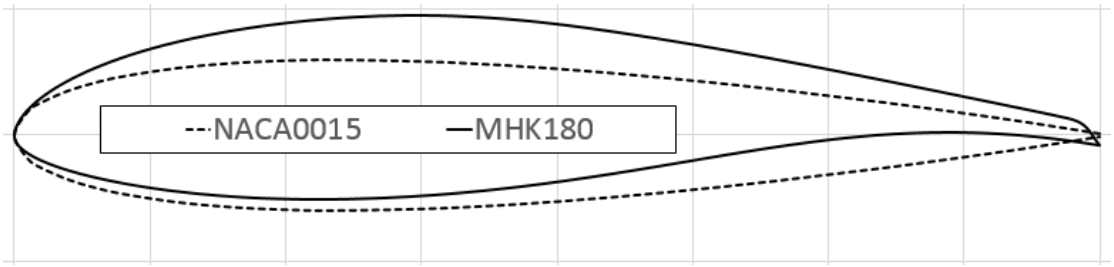

Figure 4: Comparison of airfoil shapes

The static lift and drag curves in Figure 5 give a more complete picture of the dynamics, along with data for the ms14-24 (also of the MHKF1 family) and NACA 4424 airfoils [31]. Two programs are used for the analysis, XFOIL and OVERFLOW. XFOIL models subsonic viscous/inviscid flow by a low-fidelity numerical panel method while OVERFLOW is a CFD program much like Star-CCM+ (the program used in this work). Figure 5a shows that the MHKF1 foil achieves similar performance to the ms14-24, with a peak coefficient of lift near 1.9 occurring around 14° incidence angle. Another interesting observation is that all foils achieve positive lift coefficient at zero-degree angle of incidence representative of blade camber. Figure 5b shows the drag coefficient on the x-axis which has a maximum value of 0.06. All drag values increase significantly after the static stall angle is reached, the point in each lift curve where the lift slope changes from its linear beginning. However, drag coefficient is about two orders of magnitude lower than lift coefficient (maximum drag coefficient in Figure 5 is 0.006). Although drag coefficient is an important airfoil design parameter, CFTs are lift-driven devices, thus lift coefficient has the primary influence on system response.

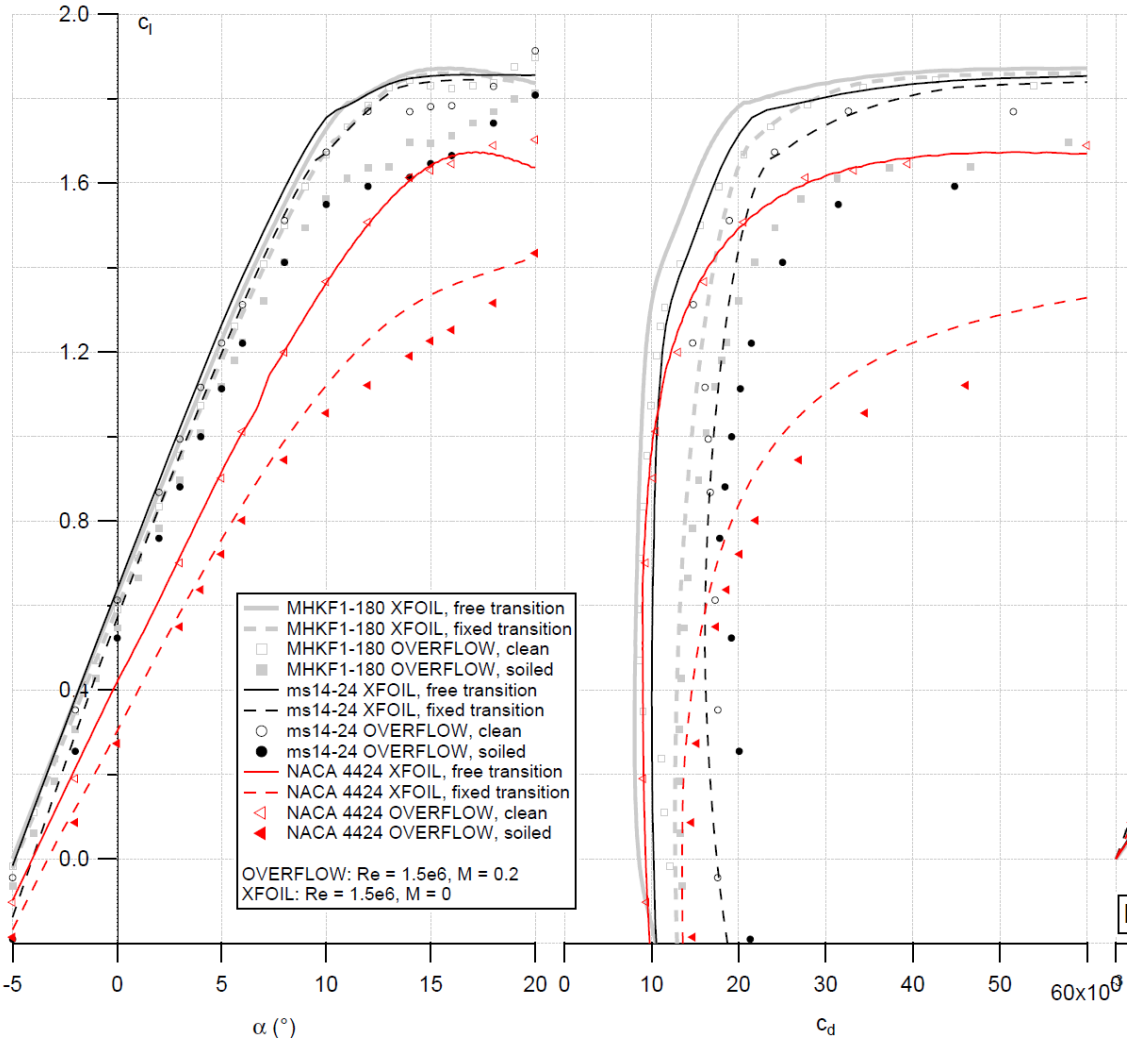

Figure 5: MHK-180F1 lift coefficient vs. a) angle of attack, b) drag coefficient [31]

Dynamic Stall

Dynamic stall (DS) is a phenomenon often mentioned but easily misunderstood. A further complication is that the methods to estimate DS are mostly semi-empirical, thus only accurate for the dataset they describe [32]. Leishman, co-creator of the Leishman-Beddoes DS model, also authored a textbook called *Principles of Helicopter Dynamics* which devotes an entire chapter to the subject of DS [33]. In the following excerpt,

Leishman holistically defines DS occurrence: "dynamic stall will occur on any aerofoil or other lifting surface when it is subjected to time-dependent pitching, plunging or vertical translation, or other type of motion, that takes the effective angle of attack above its normal static stall angle" [33].

Defining DS occurrence is particularly important for the CFT, where airfoils experience both pitching and plunging during each revolution. For airfoil speeds less than five times the input velocity ($\lambda < 5$), the airfoil's effective angle of attack often exceeds its normal static stall angle regularly; for $\lambda < 3$ the effect is even more pronounced, often described as "deep dynamic stall" [30]. However, in addition to tip-speed ratio, other factors such as airfoil type and chord-to-radius (c/R) ratio have a significant impact on DS occurrence as well. Regarding how to tell when DS occurs, Leishman proclaims that "the most distinguishing feature of dynamic stall is the shedding of a concentrated vortical disturbance from the leading edge region of the aerofoil" [32]. A helpful diagram for DS visualization is shown in Figure 6.

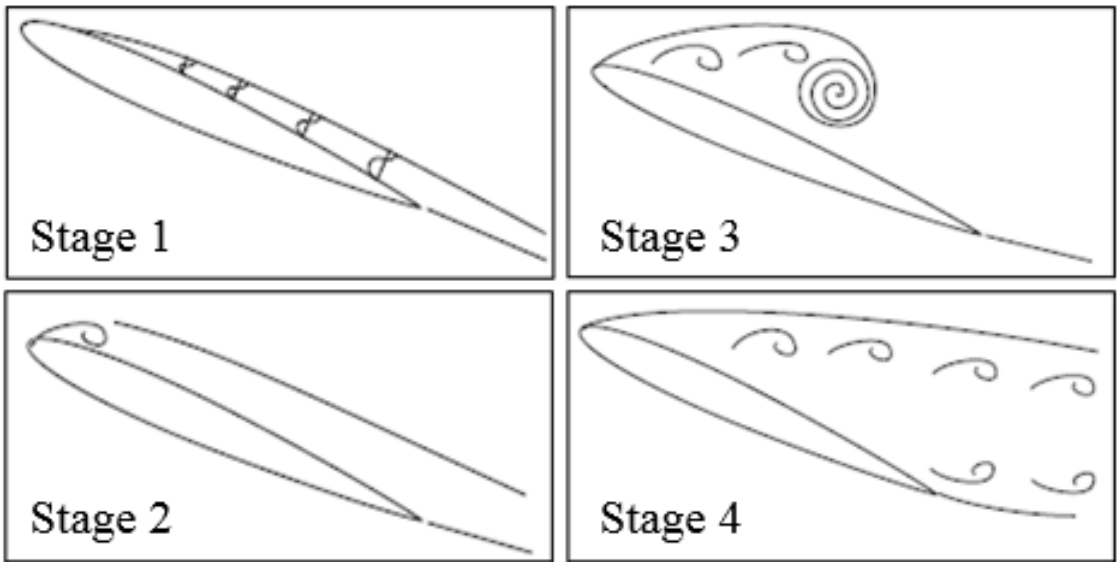

Figure 6: Dynamic stall visualization (adapted from [32])

Stage 1 is when the airfoil first surpasses the static stall angle; the circular-looking shapes on the airfoil surface (Figure 6) are flow reversals within the boundary layer. At Stage 2, flow separates from the nose (leading edge) of the airfoil at which time a small vortex starts to develop. Stage 3 is an extension of Stage 2 and exhibits the "concentrated vortical disturbance" that Leishman described. Initially, extra lift is realized because the airfoil is driven to the low-pressure vortex. Once the vortex reaches the tail (trailing edge) of the airfoil, Stage 4 brings lift stall; i.e. maximum lift is reached. Fully separated flow means that the airfoil exhibits a free-fall characteristic indicative of DS, most clearly observed by a sharp drop-off in lift. Since the CFT is a lift-driven device, it stands to reason that a drastic reduction in lift is not conducive to reliable turbine operation.

As mentioned, many semi-empirical models have been developed to describe DS, including: Boeing-Vertol, ONERA, Beddoes' Time Delay, and Leishman-Beddoes [32]. According to Leishman, these models "are not strictly predictive tools and can really be

used confidently [only] for conditions that are bounded by their validation with experimental data". Although DS models are not exact predictors, they do identify key causal factors, one of which is stall onset. Leishman writes that "The onset...is closely correlated with the attainment of…the leading-edge pressure". More recently, Sheng evaluated six different airfoil parameters to define a new stall-onset criterion, specific to low speeds as seen by CFTs [34]. He found that peak tangential force, in other words force in the direction of forward blade movement, provides a clear indicator of DS. Based on Sheng's finding, tangential force as an indicator of DS was chosen for this work; further discussion can be found in Chapter 3.

Pitch Control Application

Wind Turbine Pitch Control

Pitch control as defined in the *Wind Energy Handbook* is primarily used to regulate power but has also been effective at increasing starting torque [15]. Blade pitch, as shown in Figure 7, means that the blade nose lifts up or down about a pivot point located on the chord line between nose and tail. The angle created between the wind (or water) current and the chord line is commonly referred to as AOA (angle of attack). Pitch control was originally developed for helicopter blades and has been applied to many HAWTs.

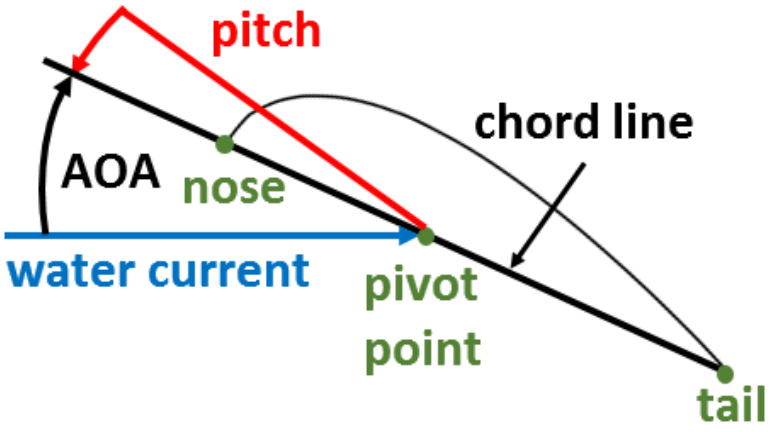

Figure 7: Blade pitch definition (only top-half of blade is shown)

There are two principal types of pitch control for HAWTs as identified in *Wind Turbine Control Systems*: pitch-to-feather and pitch-to-stall [35]. Pitch-to-feather (or blade feathering) increases the blade pitch angle while decreasing angle of attack; also, both lift coefficient (C_L) and drag coefficient (C_D) decrease. This method is most effective for avoiding high angles of attack that are associated with dynamic stall (a term defined in the next section). However, large pitch angle changes may be necessary depending on how much the wind velocity varies. Pitch-to-stall does just the opposite, decreasing blade pitch and increasing angles of attack, best suited for slowing "high speed" turbines. Of course, "high speed" depends on many factors and does not directly translate from wind to water turbines.

A 2013 study of both two- and three- bladed 600-kW research HAWTs at the National Renewable Energy Laboratory showed considerable reliability improvement using blade individual pitch control (IPC) [36]. The study by Bossanyi et al. had the primary goal to reduce blade loading, which varies with azimuthal angle, by controlling

each blade separately at any given moment. Fatigue load reductions were between 10-26% for the two-blade HAWT and 16-35% for the three-blade HAWT. Wind velocities were measured at just over 12 m/s with turbulence intensity (T.I.) just over 10%. T.I. characterizes turbulence as a percentage of the average velocity; a 10% value means that the actual velocity may *regularly* vary from 10.8 - 13.2 m/s (i.e. in the absence of extreme conditions). While most design efforts assume a constant input velocity, consideration of actual velocity by the control system may give HAWT operators more confidence that the equipment will remain within acceptable safety factors in practice.

Prior Cross-Flow Application

Multiple pitch control investigations have shown performance and reliability improvement with respect to fixed-pitch operation [7, 8, 26, 37-39]. Gorle suggested reliability improvement with little to no blade-vortex interaction [7]. Hwang et al. implemented a multi-variable parametric study and observed power increases of 70% over a fixed-pitch turbine [26]. Perhaps the most thorough inquiry was made by Lazauskas in 1992, who recognized three specific control methods: direct sinusoidal pitching, self-acting moment control, and self-acting speed control [37]. The sinusoidal control would be considered truly passive while the moment and speed control require active feedback from the system. A follow-up study in 2012 by Lazauskas and Kirke reported 50% higher efficiency and two-to-three times lower shaking force with sinusoidal control [40]. While Lazauskas observed improvement with only the first harmonic series, Vandenberghe suggested that higher-order harmonics can increase power even further [39]. A recent two-dimensional CFD study with second-order harmonic control showed 52% improvement

upon fixed-pitch, hardly more than the aforementioned first-order case [38]. A notable limitation of two-dimensional CFD is the assumption of an infinite blade span; significant blade tip losses (~40%) are reported for three-dimensional CFD [26, 27]. However, an accurate representation of the energy conversion process per unit span is attainable with two-dimensional CFD.

CHAPTER THREE

NUMERICAL METHODOLOGY

Model Validation

An extensive and thorough coverage of vertical-axis wind turbine operation exist in Ferreira's doctoral thesis, particularly with respect to CFD [2]. Wind turbine validation was chosen as opposed to water because of the larger body of knowledge and similar mechanical dynamics. Most relevant to this work, Ferreira examines three RANS models: Spallart-Almaras, k-omega (k- ω), and k-epsilon (k- ε). Spallart-Almaras has the fastest solution time of the three models because it only solves one equation for turbulence. Conversely, k- ω and k- ε each solve two equations; k- ω is better for modeling near-wall flow although Ferreira seems to prefer k- ε for bulk external flow estimation [2]. The following validation study provides rationale for model selection.

Ferreira's primary focus was the shed wake from the turbine [2]. Therefore, he chose a single blade configuration; while unpractical as a power-producing turbine, a single blade allows analysis of a longer wake that is unperturbed by additional blades. For validation, Ferreira's study was replicated, which used a wall y+ value on the order of one at the first cell layer around the NACA 0015 blade. Figure 8 shows the validation mesh for this study.

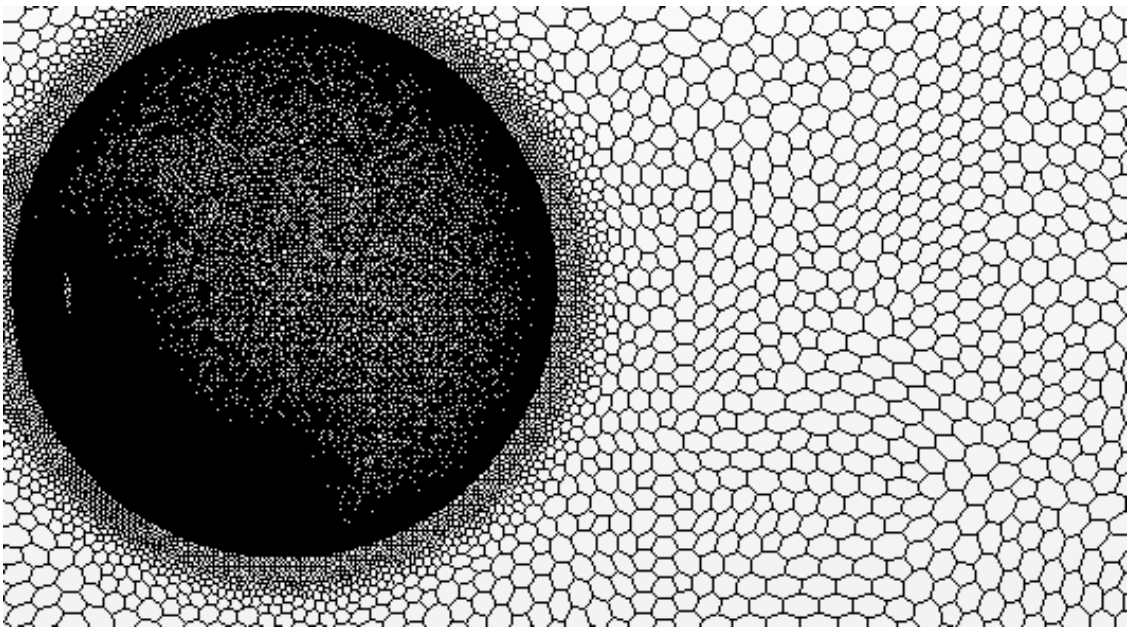

Figure 8: Validation mesh, single blade (based upon results in [2])

Hydrodynamic force upon the blade in Figure 8 is compared for the k- ε vs. k- ω models in Figure 9 (red vs. green, respectively). Ferreira showed that the force output of the models changes significantly in a CFD model during consecutive revolutions even after pseudo-steady-state conditions are reached [2]. The nature of RANS CFD produces averaging of pressure and velocity data from solving the Navier-Stokes equations that causes variation over time. For this reason, six revolutions are considered for both of the models and reflected in Figure 9. How much variation is acceptable? Figure 9 shows that normal force (solid lines) for six consecutive revolutions varies by nearly 1 x 10^4 N-m for k- ε (red), while k- ω normal force only varies by 0.2 x 10^4 N-m (green). In other words, the k- ω data shows much better precision than k- ε. For the remainder of this thesis, k- ω is the only method considered.

With precision determined, accuracy is measured in Figure 10 by direct comparison to Ferreira's data. Although Figure 9 gives force magnitude on the y-axis, Figure 10 uses force coefficient to match Ferreira's data [2]; the difference is a series of constants that do not affect this comparison. The key similarity between validation and Ferreira is that the k- ε and k- ω results show good agreement throughout the turbine revolution. That said, force coefficients between the cases vary most around 100° azimuthal angle, where k- ω has a value about 1.5 greater than Ferreira's average (Figure 10). Although the difference in magnitude is relatively large, the decision to use k- ω reflects a desire to attain repeatable results for blade force, a necessary parameter for angle of attack calculation.

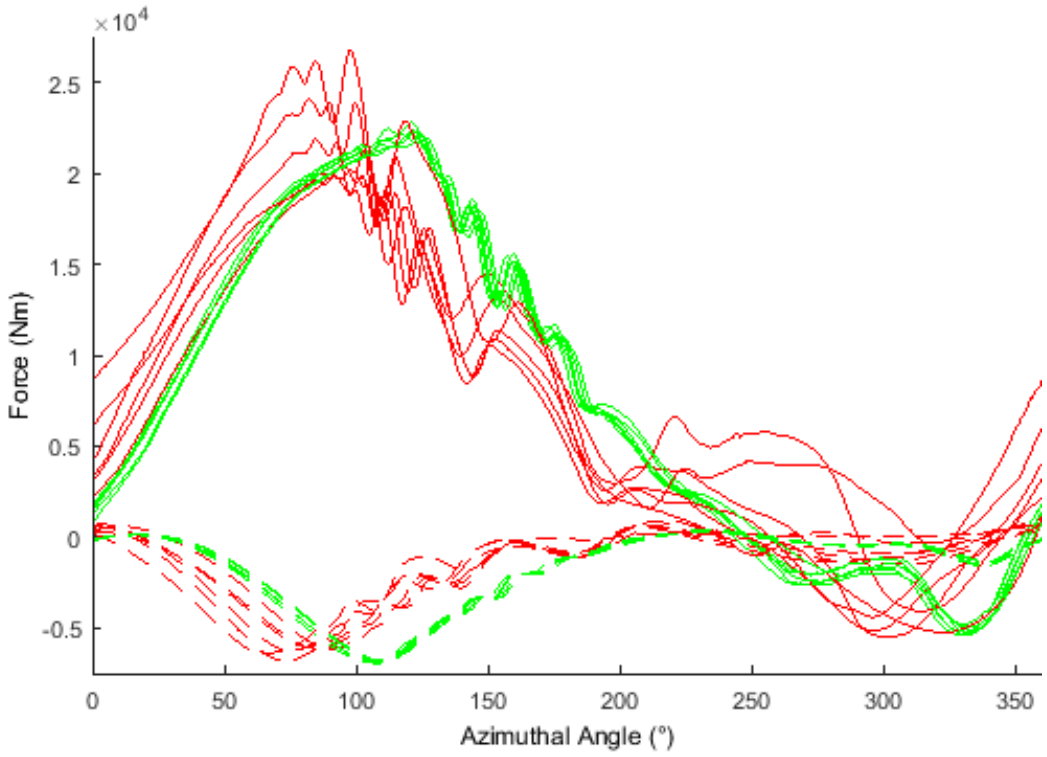

Figure 9: Validation case, six consecutive revolutions (k- ε = red, k- ω = green)

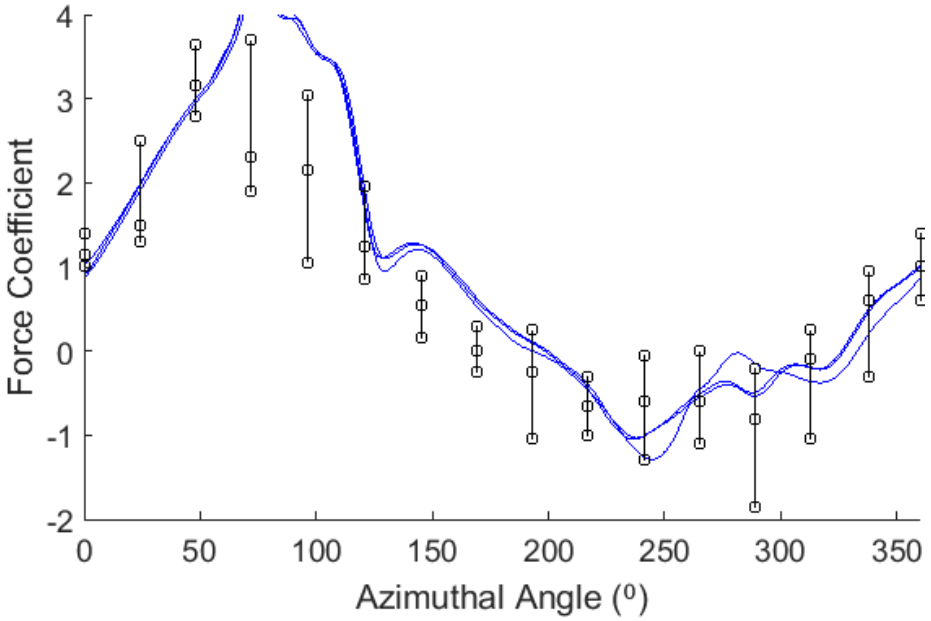

Figure 10: Comparison between k- ω turbulence model (blue) and Ferreira's data ([2])

CFT Simulation Details

The CFT studied in this thesis was based off of an existing design in the Fluids and Computations Laboratory at Montana State University. In order to keep the drivetrain from being submerged, the design features three straight blades (of type MHKF1-180) cantilevered from the spinning hub/rotor apparatus. This design also allows for testing in the Civil Engineering water flume at MSU. The turbine blades are 10 inches long with a chord length of 1.5 inches, and the turbine hub diameter is 8.5 inches. More description of the experimental design can be found in Chapter 5.

Numerical analyses were conducted with Star-CCM+, a commercial CFD program. To simplify the problem, a two-dimensional representation of the turbine (Figure 11) estimates the mid-plane of the experimental airfoils. Although 3-D simulations more

closely represent actual turbine geometries, 2-D simulations accurately estimate cross-sectional energy transfer at a much lower computational cost. The system is assumed to have constant viscosity and be incompressible. Each of the three blades is cambered toward the turbine rotor. Parameters defined in Figure 11a include turbine angular velocity ω, azimuthal angle θ (positive y-direction is zero), and water velocity U_∞. An overset mesh interface connects the stationary flume to each of the rotating airfoils; this interface allows for the mesh to reset each time-step. The total simulation mesh count is 812,790 elements. Figure 11b shows the mesh representation that coincides with Figure 11a.

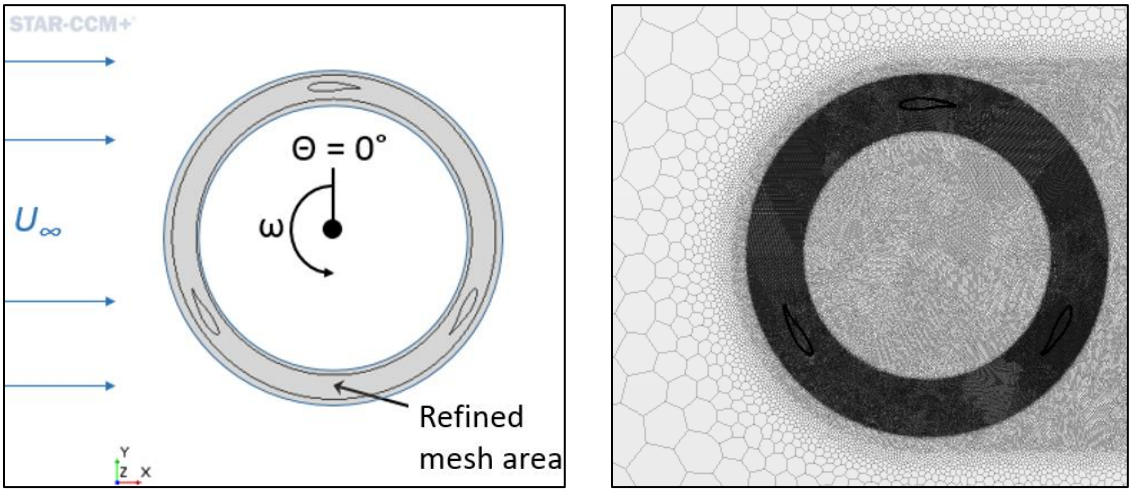

Figure 11: Two-dimensional CFT representation: a) geometry, b) mesh

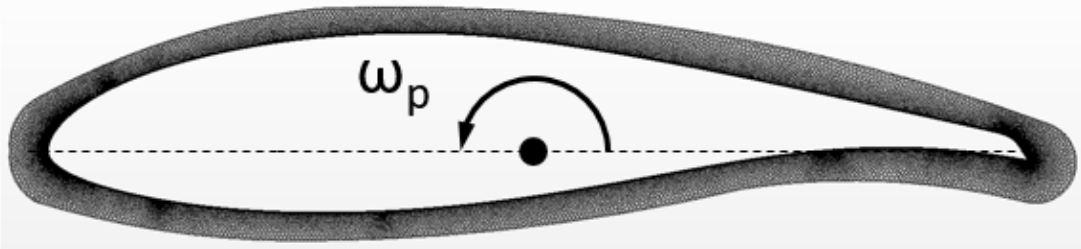

Figure 12: Airfoil mesh representation (in Star-CCM+)

The airfoil in Figure 12 features one more parameter, ω_p, angular velocity that defines pitching at blade mid-chord. Regarding the airfoil mesh, there are five prism layers closest to the surface and a cell thickness of 0.01 mm at the surface layer, 15,000 times smaller than the airfoil length of 1.5 cm. Additional properties of the surface layer include 2,151 total cells and a y^+ value on the order of one. A general definition of y^+ is the wall distance measured in viscous lengths; a value of $y^+ < 5$ allows for solution of the *viscous sublayer* [41]. The RANS k- Ω SST (Shear Stress Transport) turbulence model developed by Wilcox is generally preferred for its ability to predict near-wall flow behavior [42]. In addition to the model validation described above, it is important to note that SST turbulence allows for blending of k- ε in the bulk flow with k- ω at the wall layers. Transition between laminar and turbulent flow is estimated by the γ-Re-θ correlation [43], estimating the boundary layer by Blasius' exact solution [44].

Nominal CFT Operation

Nominal, i.e. theoretical, angle of attack profiles are defined as the angle that a symmetric airfoil experiences through one revolution [24]. Nominal angle of attack can be represented by the equation

$$\propto_n = \tan^{-1} \frac{\sin(-\theta)}{\lambda + \cos(-\theta)} \qquad (2)$$

which is dependent on two variables, azimuthal angle (θ) and tip-speed ratio (λ). Azimuthal angle gives the position of the blade with respect to the turbine rotor, while tip-speed ratio compares the CFT blade velocity and inflow velocity U_∞. A tip-speed ratio

greater than one signifies a blade velocity greater than the inflow velocity, characteristic of a lift-driven device.

XFOIL Angle of Attack

Early passive control results demonstrated that the MHKF1-180 airfoil has many subtle differences from more common airfoil types like the symmetric NACA series. In addition, Reynolds numbers under one million are not well documented because airfoils are typically designed for aerospace application. The XFOIL program developed at MIT is a popular and well-documented numerical tool to estimate airfoil lift curves [45]. The MHKF1-180 curves (Figure 14) show similarities to the previously discussed NACA curves, except for two key differences: 1) y-intercepts vary significantly based on non-symmetry, 2) negative incidence has much lower lift than positive incidence. Most importantly to this study, the new MHKF1-180 curves show that 14° may be in fact too high of an incidence angle; see Chapter 4 for results and further discussion.

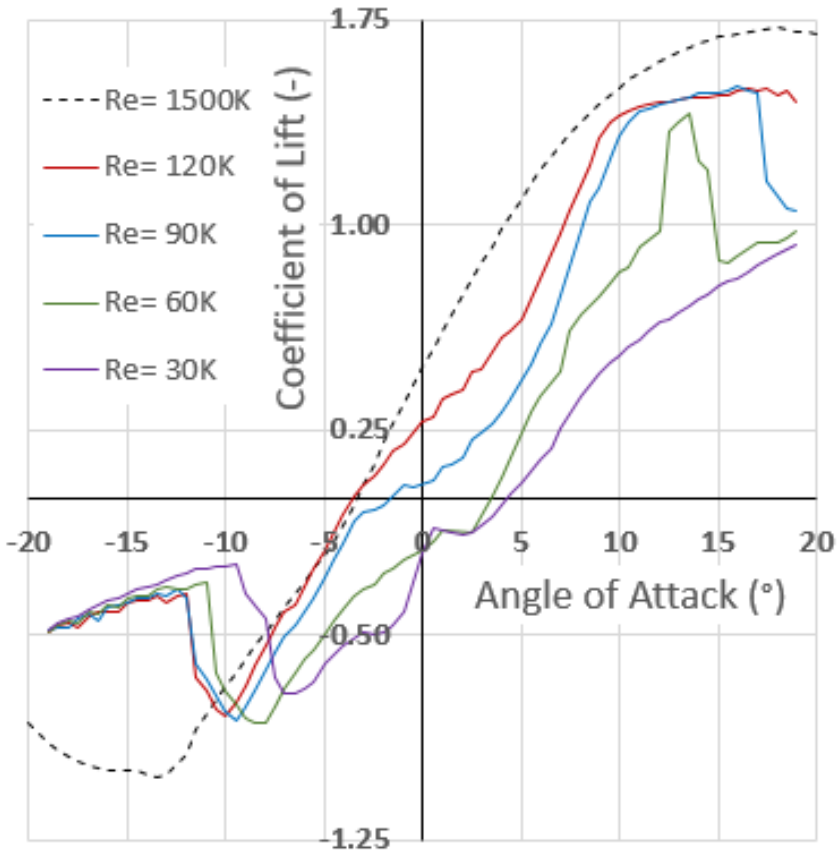

Figure 13: MHKF1-180 lift curves varying Reynolds number (in XFOIL)

Instantaneous Angle of Attack Calculation

Nominal angle of attack ($\propto_n$) gives a theoretical basis for CFT operation; however, a few of its assumptions are not valid. The first is a constant input velocity at every azimuthal angle. In reality, every CFT will experience a wake velocity deficit because energy is taken from the flow on the upstream side, thereby reducing the amount of available energy on the downstream side [8]. Furthermore, shed wake vortices create pressure and velocity disturbances that make the velocity profile very difficult to predict theoretically. While velocity perturbations aren't reflected by $\propto_n$, they can be quantified

by simulations. This section defines a new derived term called instantaneous angle of attack ($\propto_I$).

Calculation of $\propto_I$ requires some knowledge of pressure and/or velocity information for each blade at each azimuthal angle. Relative water velocity direction and magnitude are the classical choice for this calculation as they can be directly related to input velocity and the physical blade orientation [2]. However, several parameters for this study make the calculation of the local (relative) velocity non-trivial, including the relatively large c/R ratio (0.35 compared to 0.1) and the shape of the MHKF1-180 blade [30]. Another method to calculate $\propto_I$ is by measuring blade surface forces. Normal and tangential force coefficients (C_N & C_T) are calculated based on normal and tangential force (F_N & F_T) measurements where c is blade chord and ρ is density; Equation 3 shows the calculation:

$$C_{N,T} = {F_{N,T}}\Big/{\frac{1}{2}\rho(U_\infty\lambda)^2 c}\,. \tag{3}$$

With force coefficients and $\propto_n$ known, Equation 4 defines the coefficient of lift (C_L) for each blade [24]; C_L can be obtained if $\propto_n$, C_N, and C_T are known. Figure 15 gives a visual representation of Equation 4. In order to get $\propto_I$, an estimate from *Low Speed Aerodynamics* for the linear lift slope vs. angle of attack (prior to static stall) is given as 2π [46]. The 2π estimate is divided from C_L, followed by addition of the angle of attack at zero azimuthal angle ($\propto_0$), -0.0436 rad for the MHKF1-180 foil. For a symmetric airfoil $\propto_0$ is always zero; $\propto_I$ is shown by Equation 5.

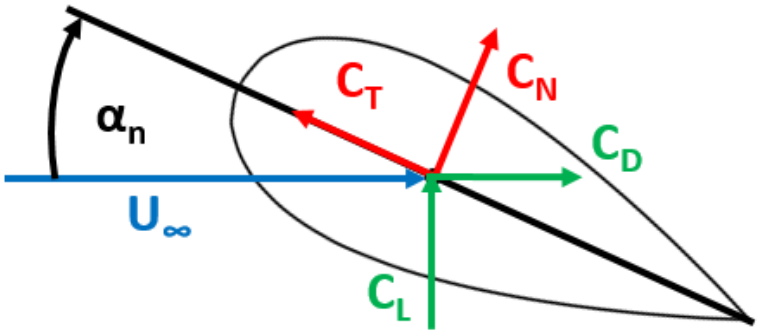

Figure 14: Free-body diagram of forces acting on a blade (not to scale)

$$C_L = C_T \sin(\propto_n) - C_N \cos(\propto_n) \tag{4}$$

$$\propto_I = C_L/2\pi - \propto_0 \tag{5}$$

Stall-Onset Angle of Attack

In Chapter 2, stall-onset criterion was identified as one of the key parameters for dynamic stall (DS) determination. Sheng analyzed six separate stall-onset indication and determined that peak tangential force was most appropriate for identifying where DS occurs [34]. For the CFT, tangential force was compared to both azimuthal angle and nominal angle of attack for the fixed-pitch case. Table 3 gives a numerical summary.

Table 3: Tangential force analysis for stall-onset criterion

λ	θ_{avg}	α_n at θ_{avg}	min α_n	% diff.
1.5	62.3	-24.0	-41.8	43%
2.0	74.3	-22.8	-30.0	24%
2.5	79.3	-20.0	-23.6	15%
3.0	89.0	-18.5	-19.5	5%

To compare all three blades, θ_{avg} is the azimuthal angle at which each blade reaches its maximum tangential force, with each curve phase-shifted to the zero azimuth and then averaged. Tangential force curves for $\lambda = 3.0$ are shown in Figure 13; "2blade" (blue curve) is phase-shifted 120° while "1blade" (green curve) is 240°, giving a θ_{avg} value of 89.0° for all three curves. Nominal angle of attack (α_n) is taken from Equation 2 at θ_{avg} and then compared to the minimum theoretical α_n by percent differencing. As expected, $\lambda = 1.5$ experiences stall well before it reaches its minimum α_n of -41.8°; it achieves a minimum value of -24.0°. The middle speeds, $\lambda = 2.5$ and $\lambda = 3.0$, exhibit reduced but significant changes (24% and 15%) in comparison. The highest speed ($\lambda = 3.0$) shows only a 5% difference between theoretical and numerical results which is probably too small to determine if DS has occurred. This exercise results in two important observations: 1) the DS onset-angle increases as tip-speed ratio decreases, 2) all cases result in a lower actual α_n than theoretical α_n, suggesting that DS may be occurring albeit with varying severity.

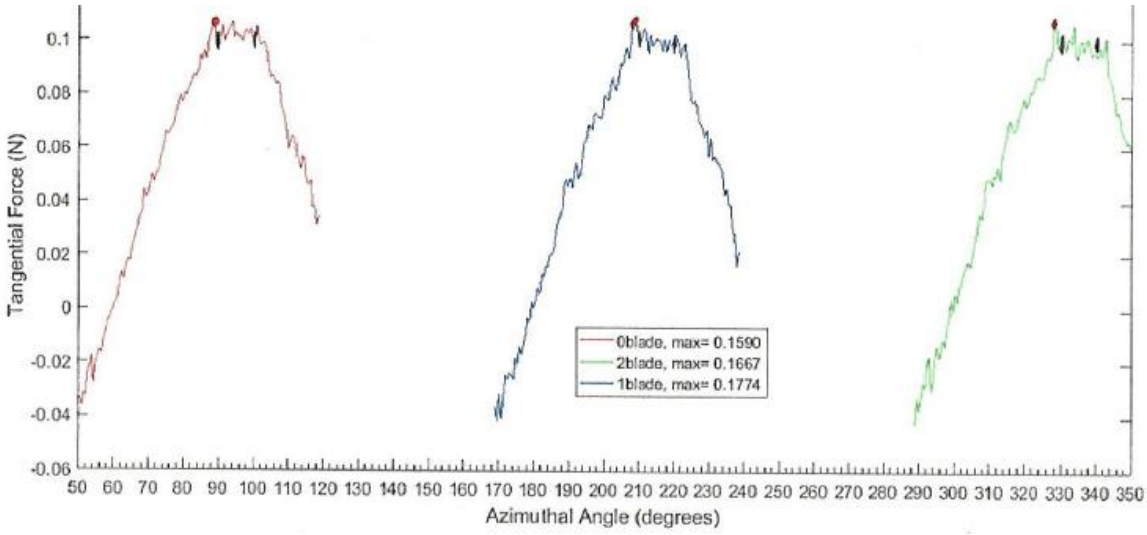

Figure 15: Tangential force curves for each CFT blade during one revolution ($\lambda = 3.0$)

Performance Calculation

Common performance metrics are coefficient of performance and coefficient of power [2, 6, 8, 34, 37]. Coefficient of power is defined as:

$$C_p = \bar{T}\omega / 0.5\rho A {U_\infty}^3. \quad (6)$$

Equation 6 introduces $\bar{T}$, the average turbine torque for one revolution. Average turbine torque represents the collective moments of the blades, where moments are defined by forward blade force times turbine radius. Numerically, the trapezoidal method is used to calculate the area under each curve as opposed to the statistical average which assumes a normal distribution; inherently this means the trapezoidal method is more accurate. Density (ρ) is 998 kg/m^3 for water and the turbine swept area (A) is $2\pi RH$. For the present study, turbine radius (R) equals 4.25 inches and blade span (H) is 10 inches.

Passive control design depends on the nominal angle of attack profile being at least close to the instantaneous angle of attack that is experienced by the blades for maximum efficacy. If this assumption is made, optimal performance could be achieved by simply forcing the cross-flow turbine to the optimal angle of attack profile, regardless of tip-speed ratio. Figure 16 shows a complete coefficient of power curve for the CFT in a no pitch configuration, with maximum power occurring at a tip-speed ratio of three. Each point shows coefficient of power from CFT simulations varying tip-speed ratio with a fixed inflow velocity of 0.72 m/s, while the 2nd-order curve fit is in fair agreement.

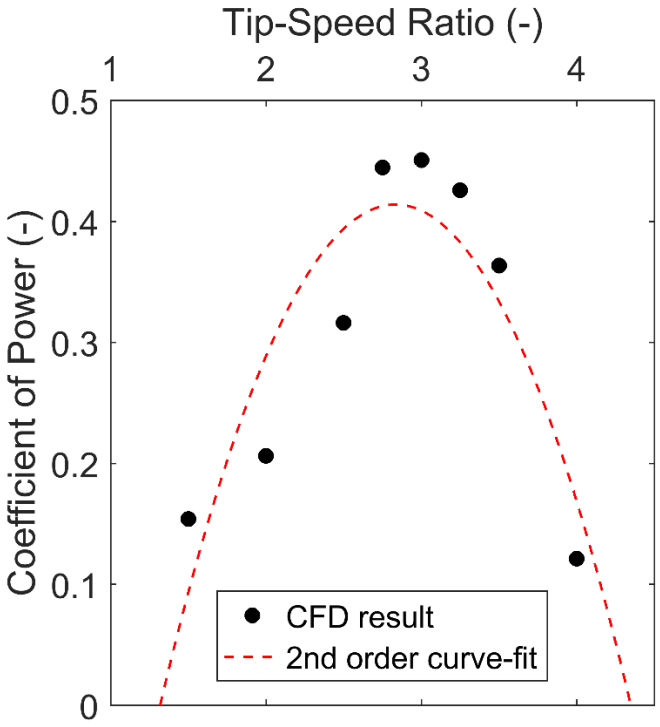

Figure 16: Coefficient of power vs. tip-speed ratio, *Baseline* (no-pitch) case

Passive Control Schemes

Nominal angle of attack ($\propto_n$) is held below an angle indicative of stall onset by way of pitch control (also known as feathering for HAWTs). This strategy was also used previously by Staelens for vertical-axis wind turbines [47]. While Staelens explored a sinusoidal pitch case, he only considered one tip-speed ratio ($\lambda = 2.9$). Because stall is generally less prevalent for $\lambda > 2.9$, this work considers only low tip-speed ratios. The four λ values considered in this work are 1.5, 2.0, 2.5, and 3.0, all with a constant input velocity, U_∞= 0.72 m/s. A graphical representation for $\propto_n$ is shown in Figure 17, which defines the *Baseline* case to improve upon with pitch control. Three distinct passive pitch control strategies are created by modification of the $\propto_n$ curves: *Limit*, *Harmonic*, and *Scale*. *Limit*

keeps $\propto_n$ within $\pm$14° to avoid dynamic stall and improve power output. *Harmonic* and *Scale* also obey the $\pm$14° angle of attack, but are derived to provide a continuous motion of pitching to mitigate unnecessary controller impulse.

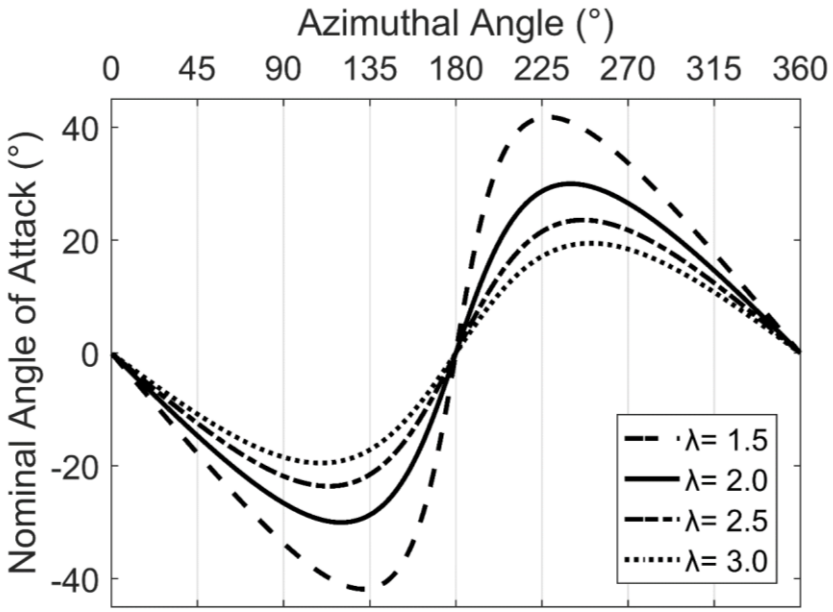

Figure 17: Theoretical angle of attack, *Baseline* (no-pitch)

Limit

Modification to $\propto_n$ as a result of pitch control is first done with the *Limit* control. The *Limit* control prevents the blades from exceeding pre-defined limits on their local angle of attack. Equation 7 gives the nominal *Limit* angle of attack ($\propto_{n,L}$) dependent upon Equation 2 ($\propto_n$):

$$\propto_{n,L} = \begin{cases} \propto_n \ if \ \propto_n < \left|\pm 14^\circ\right| \\ \pm 14^\circ \ if \ \propto_n \geq \left|\pm 14^\circ\right| \end{cases}. \tag{7}$$

where $\pm 14°$ is chosen to be near the static stall angle for the MHK-180F1 airfoil. The mathematical definition of *Limit* control is easily prescribed, but graphical representation (Figure 18) suggests a major obstacle to its success. Since *Baseline* only exceeds $\pm 14°$ intermittently, start-stop motion of the control is required as suggested by the piecewise-continuous nature of Equation 7. This start-stop motion requires unnecessary blade acceleration especially around 180° azimuthal angle.

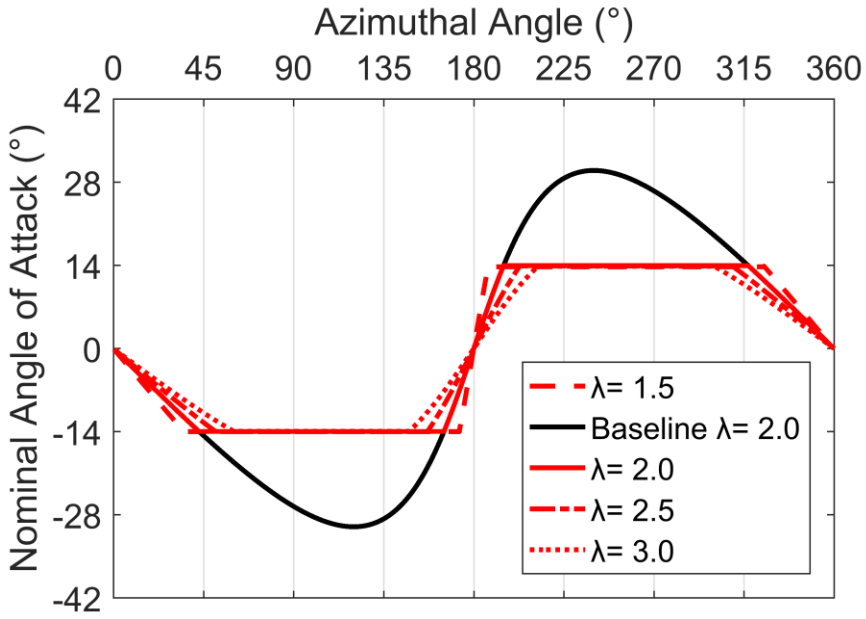

Figure 18: Theoretical angle of attack, *Limit* ($\propto_{n,L}$)

Harmonic

The *Harmonic* scheme is defined based on both the *Limit* attempt and previous success of sinusoid-based controls [37-39, 47]. Paillard et al. considered first, second, and third harmonics functions, with the conclusion that the second-order harmonic produced

the most power [38]. The *Harmonic* nominal angle of attack ($\propto_{n,H}$) is represented in Equation 8 as $\propto_{n,H} = \propto_n + \gamma \sin(\theta) - \frac{1}{2}\gamma \sin(2\theta)$ (8)

where pitch magnitude (γ) is the only new variable. The highest γ is 27° for λ= 1.5 and the lowest is 5° for λ= 3.0. Figure 19 graphically shows how the *Harmonic* control ($\propto_{n,H}$) keeps angle of attack near $\pm$14° for almost half of the turbine's revolution, therefore the airfoil maintains optimal lift for a longer period of time. An obvious exception is seen for λ= 1.5 which oscillates between $\pm$5° and $\pm$14°, unavoidable by Equation 8. This reduction in angle of attack lowers performance making *Harmonic* sub-optimal for λ= 1.5.

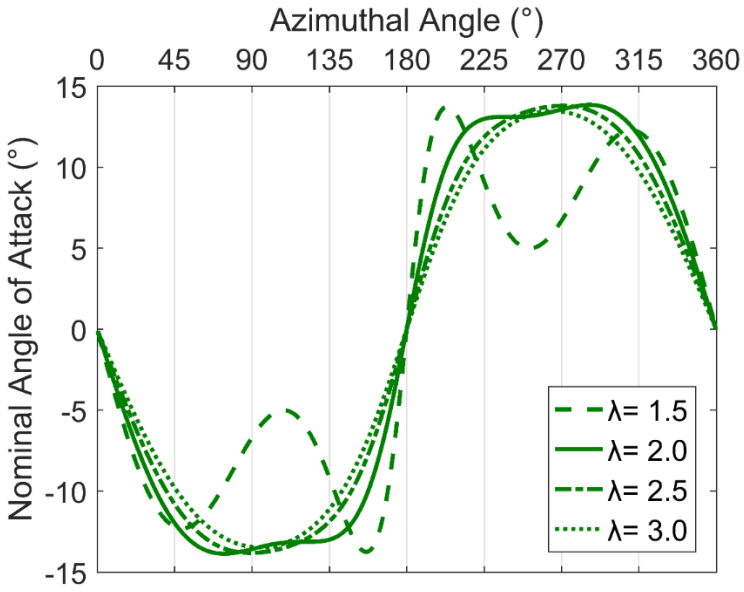

Figure 19: Theoretical angle of attack, *Harmonic* ($\propto_{n,H}$)

Scale

The third control, *Scale,* has an angle of attack profile defined by

$\propto_{n,S} = \beta \propto_{n,}$ (9)

where $\propto_n$ (again described by Equation 2) is simply multiplied by an amplifier (β) that can take a value between zero and one. An amplification of zero means that the blades would pitch to zero angle of attack, while an amplification of one means no pitching (assuming nominal and instantaneous are equal). For the 14° amplitude, minimum β= 0.33 for λ= 1.5 while maximum β= 0.71 for λ= 3.0. *Scale* takes longer than the other two pitch cases to travel from zero azimuthal angle to peak nominal angle of attack ($\propto_n$), meaning that it may have lower performance overall. However, changing $\propto_n$ linearly imposes the simplest pitch algorithm of the three schemes, and Figure 20 shows that *Scale* control gives a better result for λ= 1.5 than *Harmonic*.

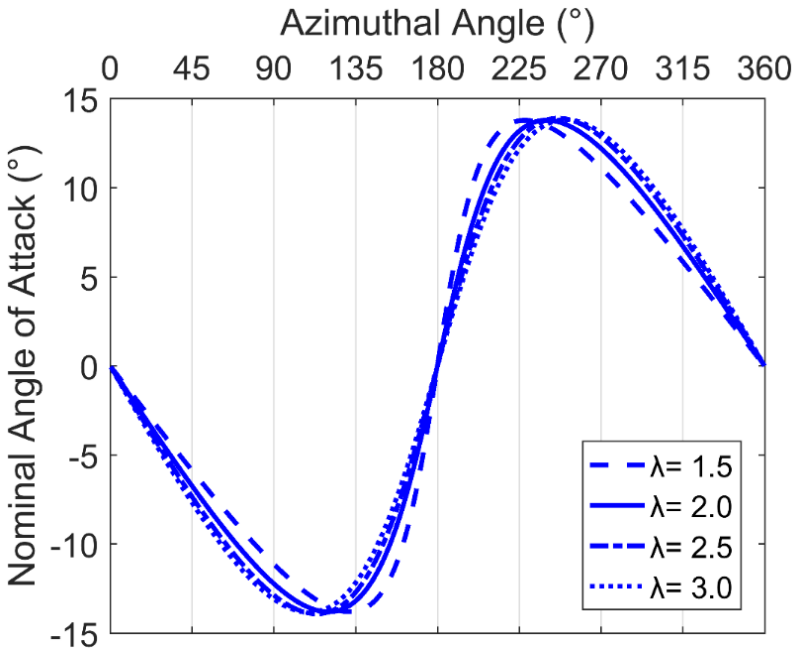

Figure 20: Theoretical angle of attack, *Scale* ($\propto_{n,S}$)

The simplistic form of *Scale* control makes it the most convenient to explore amplitude amplification. Figure 21 shows variable amplitude values corresponding to the

nominal angle of attack values for a tip-speed ratio of three. In this case, a 14° amplitude equals $\beta = 0.71$, while a 10° amplitude equals $\beta = 0.5$. While determining the "best" amplitude is not the primary focus of this work, Figure 21 clearly shows how modification of pitch amplitude can be modified to cater to any CFT with any airfoil type. For example, this study considers a CFT with a chord-to-radius ratio of 0.352 and the airfoil type MHK-180F1. Many CFTs have a chord-to-radius ratio around 0.1 and a symmetric NACA airfoil, therefore they may require slightly different amplitude limits if pitch control is to be considered [30].

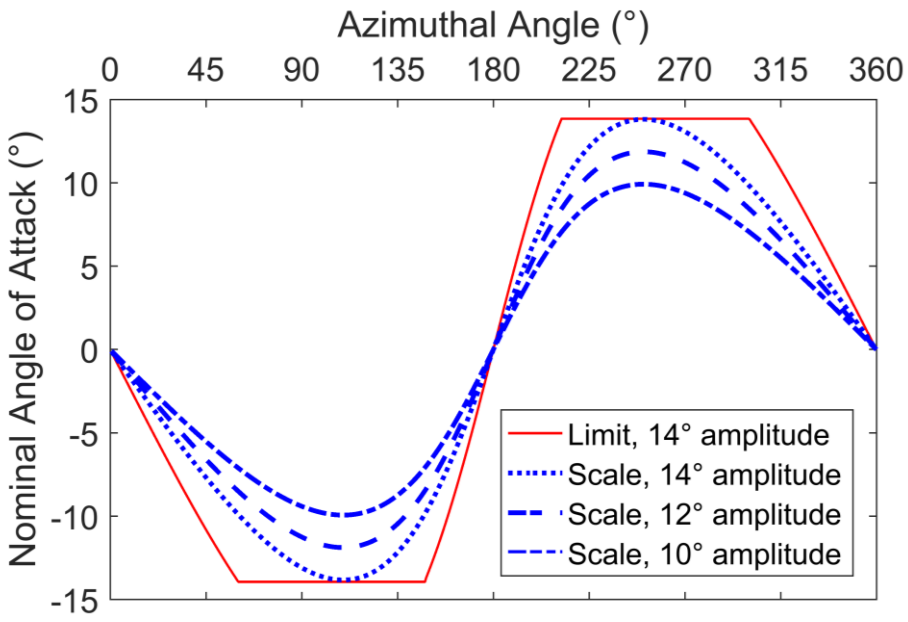

Figure 21: *Scale* ($\propto_{n,s}$) varying amplification, $\lambda = 3.0$

Active Control Schemes

Every power-producing CFT will experience a wake velocity deficit because energy is taken from the flow on the upstream side of the turbine, thereby reducing the

amount of available energy on the downstream side [8]. Furthermore, shed wake vortices create pressure and velocity disturbances that make the velocity profile very difficult to predict theoretically. As discussed previously, active pitch control allows the CFT real-time adjustment ability to flow conditions. This section gives a preliminary attempt at active control that, while only scratching the surface as a potential control strategy, chronicles findings and observations that may lead to future investigation.

An early implementation of proportional-integral-derivative (PID) control with respect to hydrokinetics was Sperry's automatic ship steering mechanism developed in 1922 [48]. Since then, PID control has become an industry standard in large part because it can be applied to a wide range of processes. The basic function of a PID control is to take a process value (system input) and drive it to a desired set point. Specific to renewable energy, advanced PID control systems have been extensively developed for horizontal-axis wind turbines primarily for torque and speed control [35, 36]. To understand PID control, all its components must be considered: proportional, integral, and derivative. Proportional control represents the gain of the controller; too much gain will cause overshoot but too little gain will prevent full adjustment to optimal conditions. To compensate, integral control eliminates steady-state error associated with the proportional controller, but can cause overshoot due to accumulated error [36]. Derivative control can improve stability of the system by incorporating the rate at which the system is minimizing the error between the present state and desired output, but is not always used in practice. For this work, only proportional control is considered based on Westcott's assertion that integral and derivative control can drive a system to instability

with incorrect values [49], and the researcher's lack of experience in the area. Proportional-only control provides useful findings that may serve as a foundation for future optimization.

The (passive) *Scale* control is chosen for active implementation because it is a simpler algorithm mathematically than *Harmonic* control and achieves nearly the same performance benefits for the cases tested (see Chapter 4). Where *Harmonic* uses pitch magnitude γ with two separate terms (Equation 8), *Scale* only has amplification factor β with one term (Equation 9). Theoretically β could be defined solely by variation in the relative flow velocity that the blade experiences at each azimuthal angle. However, without knowing the relative flow velocity explicitly, it is difficult to determine what β should be. Convergence of the numerical solution provides a challenge as well; too much pitch made the simulation crash while too little pitch didn't yield a useful result. A compromise to both avoid non-convergence and obtain a valuable solution is made by splitting β into two separate parameters, βi and βe. The initial value, βi, is based on passive control, while βe is determined by the error between nominal and instantaneous angle of attack as shown in Equation 10. Equation 11 gives the active angle of attack based on deviation of instantaneous angle of attack from the *Scale* path ($\propto_{n,S}$).

$$\beta e = Kp \times \left(\left[\alpha_I - \alpha_{n,S}\right]/\alpha_{max}\right) \tag{10}$$

$$\propto_{n,A} = (\beta i + \beta e) \propto_n \tag{11}$$

The new parameters, maximum angle of attack (α_{max}) and gain constant (Kp), relate error to the system requirements. A constant (maximum) angle of attack value ensures a consistent value for βe, while gain constant Kp varies the effect of βe on pitch

response. For stability, βe is limited in the preliminary results to ±0.2. The plus-or-minus indicates whether pitch should be increased or decreased, while 0.2 equates to 20% of the range (0 to 1) for a net potential change of 40%. Future optimization may necessitate elimination of either the 40% limitation or the initial value βi so that there is not unnecessary redundancy in the system.

An initial attempt to rapidly model these control systems outside of CFD simulation was made interpolating XFOIL airfoil data within MATLAB. The idea was to reduce solution time by low-fidelity modeling; once optimized that way, a few select conditions could be modeled in CFD. Ultimately this effort did not provide enough accuracy to be particularly useful, largely due to the difficulty in predicting dynamic stall. Results for tip-speed ratios of 2.0, 2.5, and 3.0 can be found in Appendix B.

CHAPTER FOUR

NUMERICAL RESULTS

Passive Control

The bulk of results in this thesis consists of the following passive pitch control evaluation, which includes the three control systems (*Limit*, *Harmonic*, and *Scale*) evaluated over four tip-speed ratios. Performance gain is shown in Figure 22, where the best result is a 249% percent difference by *Harmonic* (relative to *Baseline*) at $\lambda = 2.0$. This section consists of selected low- and high- speed results; however, coefficient of power and turbine thrust data (Tables 3-5) compare all tip-speed ratios.

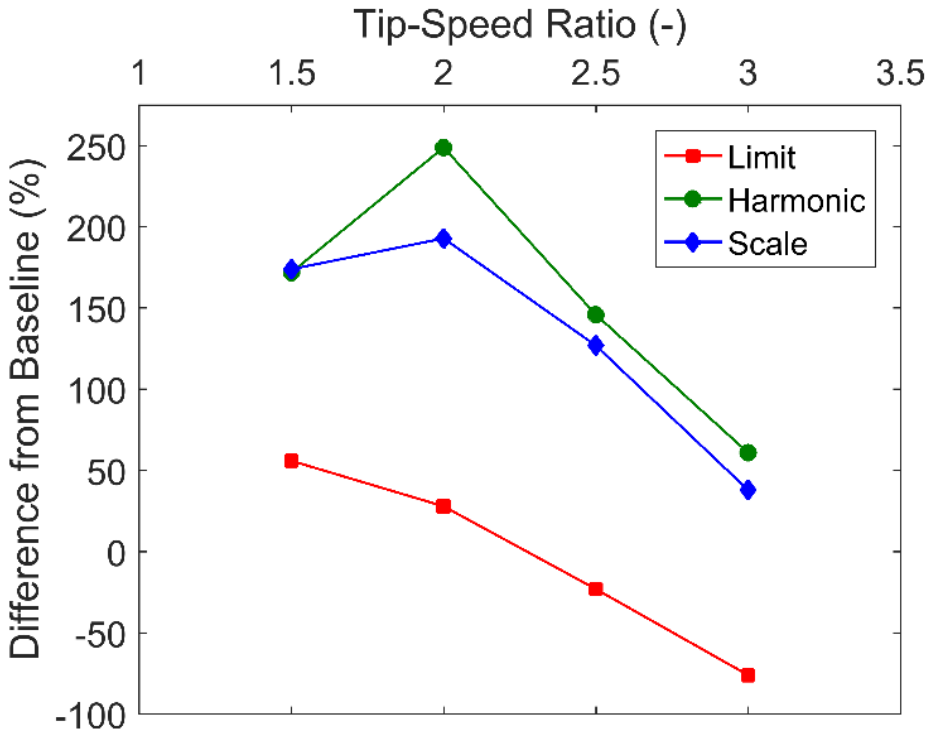

Figure 22: Incremental performance gain by pitch control, all cases

Instantaneous Angle of Attack

To evaluate effectiveness of the controls, instantaneous angle of attack ($\propto_I$) curves show system response relative to the no pitch (*Baseline*) case. To analyze control scheme efficacy, instantaneous angle of attack ($\propto_I$) curves are shown in Figure 23 for $\lambda = 2.0$, along with the minimum angle achieved by each control. *Baseline* exhibits classic characteristics of dynamic stall, including a sharp peak followed by a shelf and precipitous drop between 45-225°. Control schemes undoubtedly mitigate dynamic stall, with *Limit* the most definitive, starting at ~45°. However, *Limit* stays in the negative $\propto_I$ range for most of the downstream (180-360°) pass which doesn't seem to provide any benefit. *Harmonic* and *Scale* both mitigate dynamic stall on the upstream side while mimicking *Baseline* for the most part downstream. Minimum $\propto_I$ are well in exceedance of the $\pm 14°$ limit, but the primary goal of limiting $\propto_I$ to avoid dynamic stall is definitively achieved.

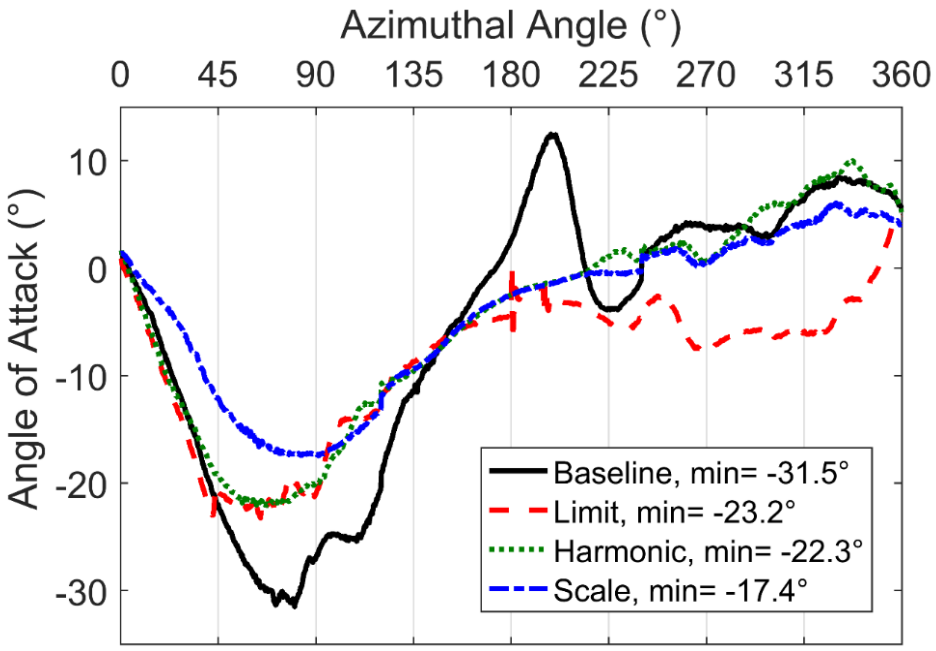

Figure 23. Instantaneous angle of attack, $\lambda = 2.0$

Figure 24 for *Baseline* with a tip-speed ratio of three shows no clear sign of dynamic stall, as it peaks only 3.5° lower than the control limit. In comparison, all control schemes peak within 1.2-1.6° of the 14° limit. *Limit*, however, diverges from the other controls on the downstream side; this is the most likely explanation for its relative power conversion inefficiency, to be discussed with Turbine Performance. Also, *Scale* with variable amplitude is shown in Figure 25. The upstream (0-180°) angle of attack in Figure 25 shows good agreement with the variance in amplitude, though downstream suggests little change.

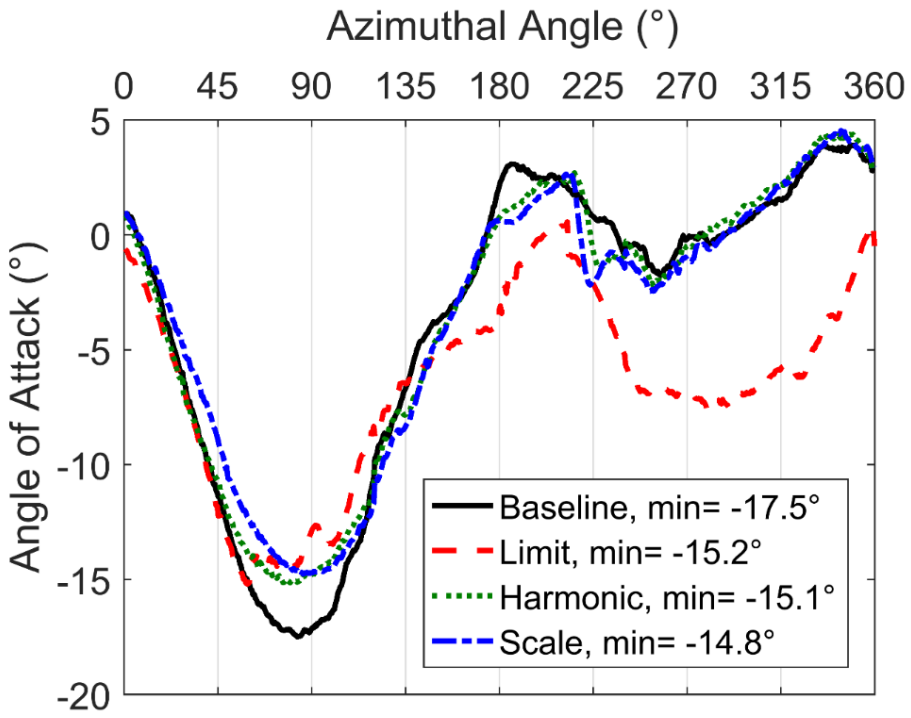

Figure 24: Instantaneous angle of attack, λ= 3.0

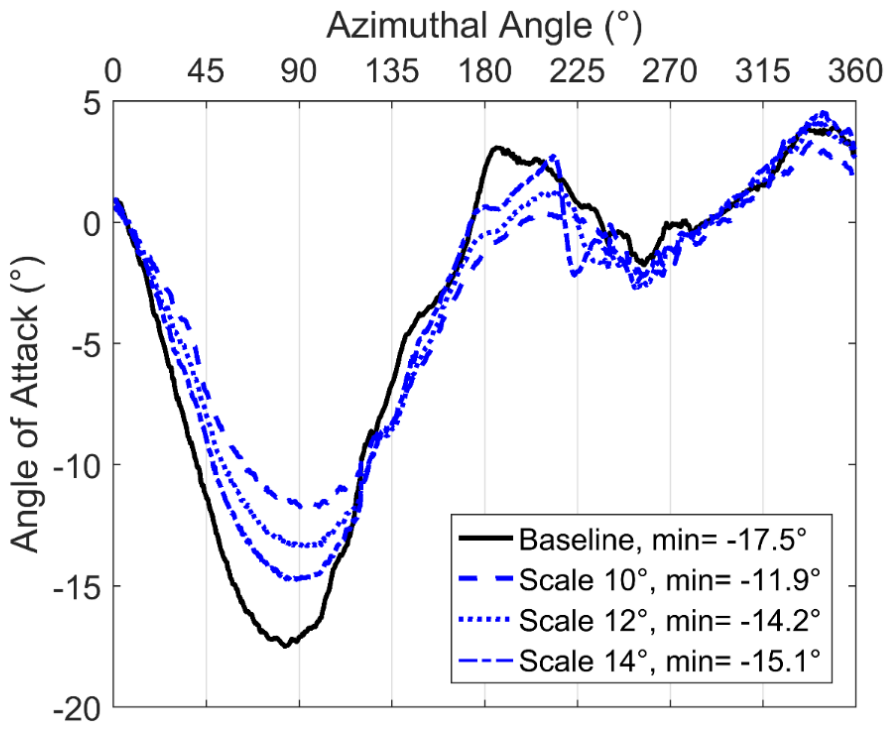

Figure 25: Instantaneous angle of attack varying amplitude, λ= 3.0

Turbine Performance

Figure 26 shows turbine torque for λ= 2.0. All curves show three separate peaks within one revolution, analogous to the periodic motion of each blade. The *Baseline* and *Limit* cases exhibit significant periods of negative torque that diminish power production. In contrast, *Harmonic* and *Scale* show a considerable reduction in negative torque occurrence. Also, both *Harmonic* and *Scale* peak about 0.5 N-m higher than *Baseline* with a phase shift of approximately 10°. In terms of reliability, *Harmonic* and *Scale* seem to only improve upon the *Baseline* torque curve considering that the peak-to-trough slopes are slightly steeper for *Baseline*. This means that in addition to the increase in power that both *Harmonic* and *Scale* provide, they appear to require no additional reliability consideration, even though performance and reliability are often directly at odds.

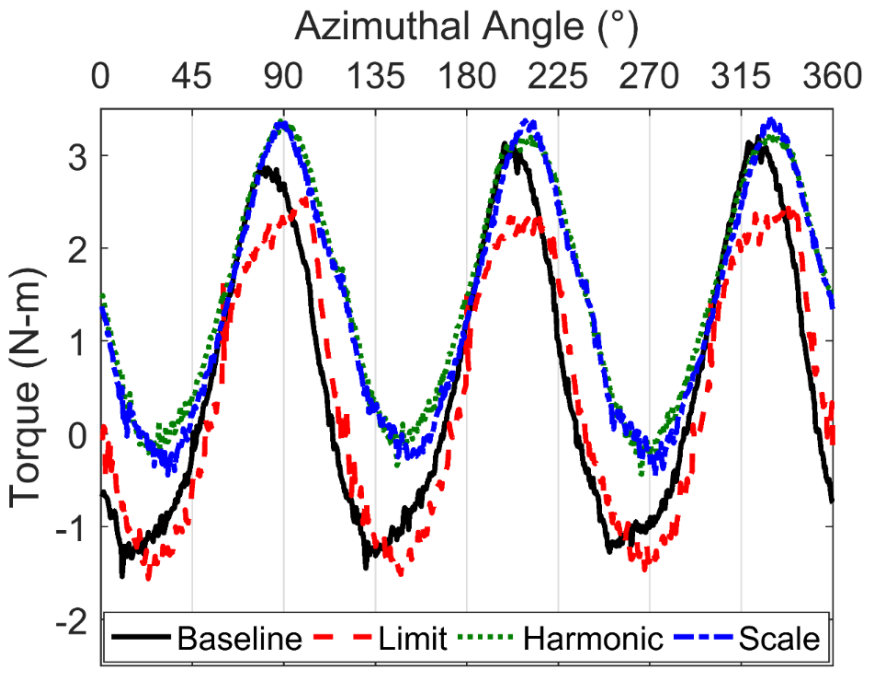

Figure 26. Total turbine torque, λ= 2.0

Figures 27 and 28 show turbine torque for a tip-speed ratio of three during one revolution. Though each of the curves show significant periods of negative torque that diminish power production, the *Baseline* and *Limit* cases have the largest negative area. In contrast, *Harmonic* and *Scale* maintain a positive torque through the majority of a revolution. Figure 28 shows the *Scale* case only with varying magnitude of β to achieve nominal angle of attack from 10-14° as shown in Figure 25. Varying amplitude signifies the ability to optimize each control to an ideal angle of attack as mentioned in Chapter 3.

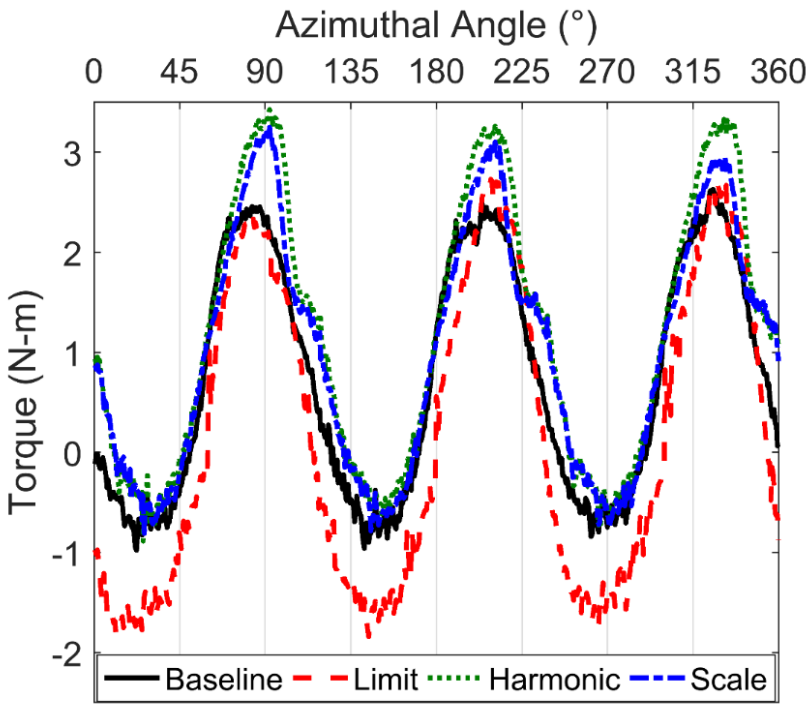

Figure 27: Total turbine torque, 14° angle limit, λ= 3.0

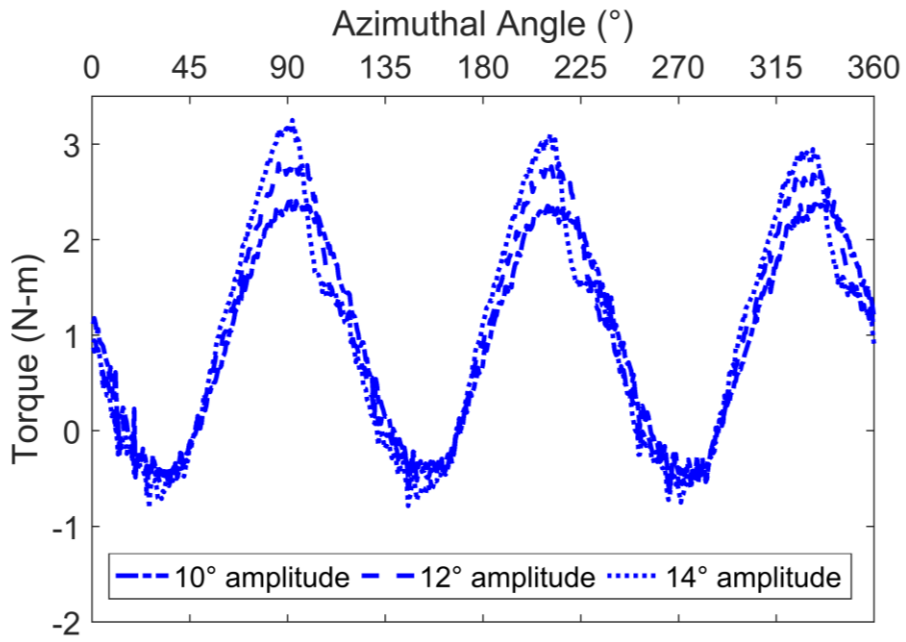

Figure 28: Total turbine torque, *Scale* control only, variable angle limits

Table 4 provides coefficient of power (C_p) per unit span values for all cases. Two expectations are confirmed: 1) performance gains induced by pitch control are greatest at lower tip-speed ratios, 2) both *Harmonic* and *Scale* consistently perform better than *Limit*, likely a consequence of *Limit* a piece-wise (not fully continuous) function. Although power output for the *Baseline* are highest in Table 3 at $\lambda = 3.0$, all pitch cases exhibit considerable decreases in output from $\lambda = 2.0$ to $\lambda = 3.0$, suggesting that pitch control yields diminishing returns as a CFT approaches its optimal tip-speed ratio for performance.

Table 4: Coefficient of power per unit span (m^{-1}, all cases)

	Baseline	**Limit**	**Harmonic**	**Scale**
Λ				
1.5	0.0392	0.0610	0.1065	0.1072
2.0	0.0525	0.0674	0.1831	0.1534
2.5	0.0804	0.0616	0.1974	0.1822
3.0	0.1145	0.0269	0.1848	0.1586

Figure 29 shows the coefficient of power values graphically, with 0.254 m (10 inches) as the blade length, for *Baseline* and *Harmonic*. The *Harmonic* result suggests a coefficient of power near 0.8 possible for $\lambda = 2.5$, about 30% greater than the Betz limit of 0.593. This result may be exaggerated because the volume mesh in Star-CCM+ might be insufficient to effectively capture the transition from blade boundary layer flow to freestream flow. While this work was focused on modeling the CFT and not on best practices of meshing, a mesh convergence study would be beneficial in light of this result. Nonetheless, the same mesh was used for both *Baseline* and *Harmonic*, where it is clear that *Harmonic* provides considerably higher power than *Baseline.* *Harmonic* also peaks

earlier than *Baseline* with respect to tip-speed ratio and shows great agreement with a 2nd order curve-fit. The significance of an earlier peak is that *Harmonic* seems best suited for the "deep-stall" range ($\lambda < 2.0$).

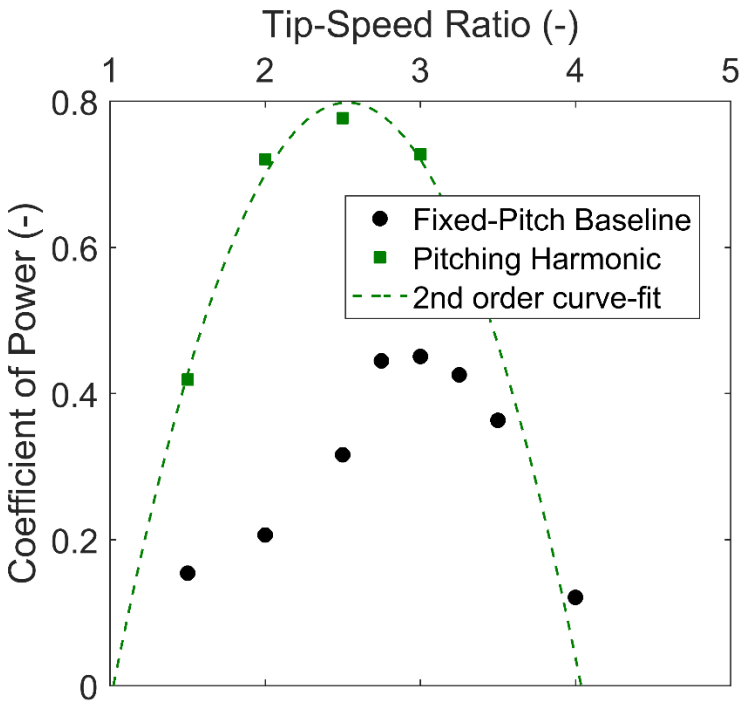

Figure 29: Coefficient of power vs. tip-speed ratio, *Harmonic*

Turbine Thrust

The net effect of water force on all of the blades is reflected by turbine thrust, both parallel with and perpendicular to the flow direction. Figure 30 shows the total turbine thrust in both directions. The parallel thrust shows mostly positive values, while the perpendicular thrust shows positive and negative values indicative of the blades moving the turbine from side to side, also known as shaking force.

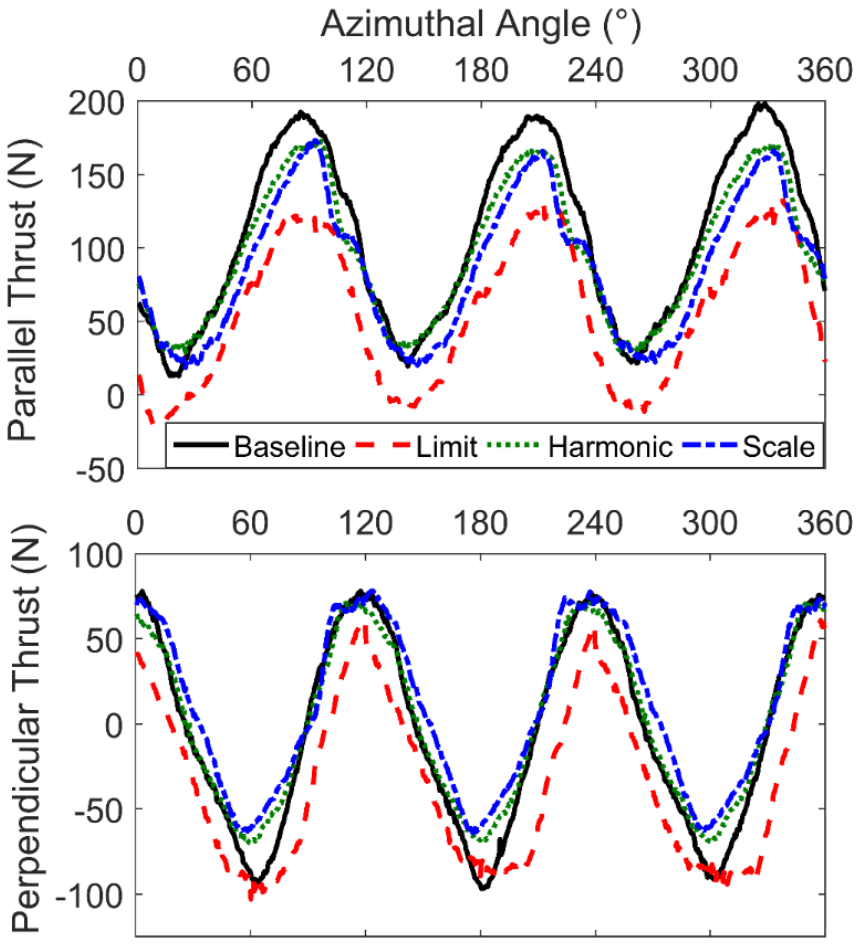

Figure 30: Total turbine thrust, λ= 3.0

Tables 5 and 6 show the total amplitude (peak-to-trough) in parallel and perpendicular thrust. All cases show significant parallel thrust reduction relative to *Baseline,* with percent reduction ranging from 20-333%. The same can generally be said for perpendicular thrust, except for *Limit* at λ= 2.5 which sees a slight 10% increase. These massive reductions in thrust make sense because dynamic stall drastically increases the force loading on individual blades, reflected by *Baseline* $\propto_I$ in Figure 23. Therefore, reducing the hydrodynamic influence of dynamic stall on the CFT simultaneously reduces the hydrodynamic loading on the blades and turbine structure. This considerable change

in thrust loading due to pitch control seems to be a significant secondary benefit, particularly for low tip-speed ratios.

Table 5: Turbine thrust total amplitude parallel to inflow (in Newtons)

	Baseline	**Limit**	**Harmonic**	**Scale**
λ				
1.5	99.1	48.8	46.9	22.9
2.0	143.0	68.9	60.9	56.5
2.5	175.4	111.2	104.5	107.8
3.0	185.4	154.7	145.4	154.8

Table 6: Turbine thrust total amplitude perpendicular to inflow (in Newtons)

	Baseline	**Limit**	**Harmonic**	**Scale**
λ				
1.5	90.9	92.7	73.8	28.5
2.0	167.6	121.7	81.5	56.1
2.5	129.8	143.5	96.8	89.9
3.0	174.9	164.8	142.0	142.3

Velocity Field Visualization

Figure 31 shows the velocity field for λ= 1.5, the lowest tip-speed ratio tested. Ux is defined here as the x-component of velocity while Uin is the constant inflow velocity (0.72 m/s). *Harmonic* and *Scale* (Figure 31c and 31d) show development of high- and low-velocity areas throughout their wakes. Dark areas represent the turbine wake while lighter areas indicate faster flow having accelerated around the reduced cross-sectional area caused by the CFT and flume walls. These areas seem to separate from the blades more completely than for *Baseline* and *Limit* (Figure 31a and 31b). Also, overall thrust in the flow direction (Table 5) is substantially reduced, even with the larger flow structures for

Harmonic and *Scale*. This is likely a result of both the total number of shed vortices and the rate at which they separate from the blades. While the result for *Harmonic* and *Scale* shows greater power output potential (Table 4), *Limit* control may be more desirable in an array-type configuration due to faster re-energization of the wake [14]. These flow variations also help explain why instantaneous angle of attack ($\propto_I$) deviates significantly from nominal ($\propto_n$); $\propto_n$ assumes that input velocity is equal throughout the turbine revolution. Figure 31 leaves no doubt that vortices shed from upstream (left hand side) blades alter the velocity field, thereby impacting the downstream conditions.

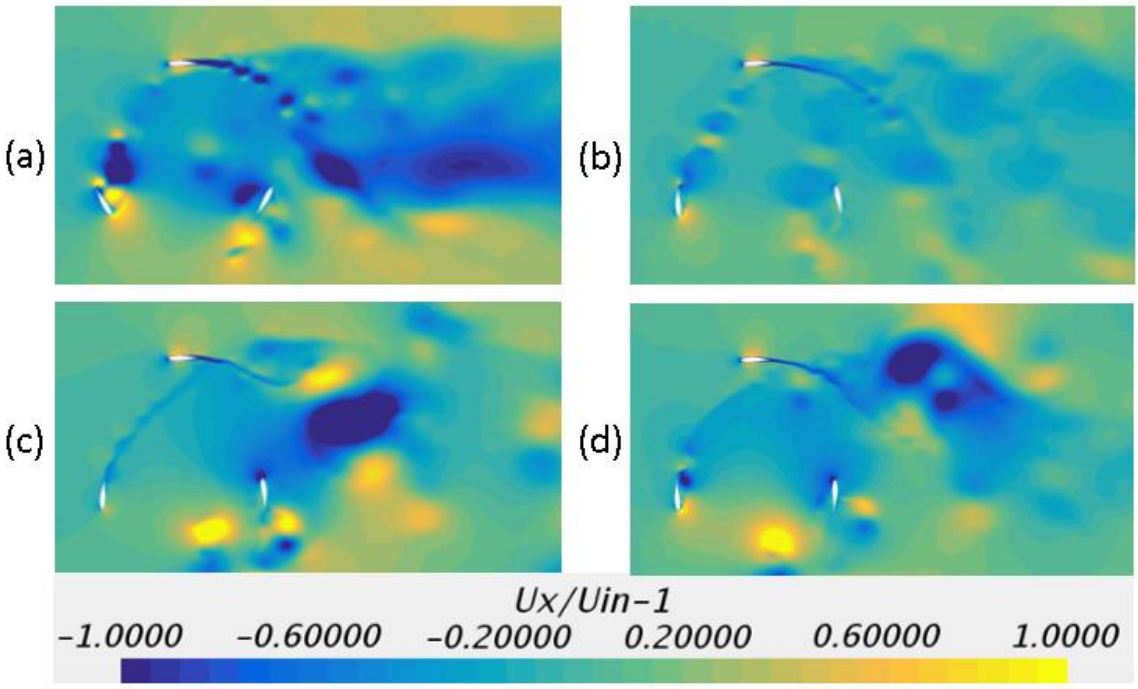

Figure 31. Non-dimensionalized x-velocity perturbation field, λ= 1.5 ((a) *Baseline*, (b) *Limit*, (c) *Harmonic*, (d) *Scale*)

Flow Field Quantification

Additional equations are required to quantitatively analyse flow field data. Non-dimensional vorticity and blade surface pressure coefficient are defined by Equations 12 and 13.

$$\Omega_{nd} = \Omega c / \lambda U_{\infty} \quad (12)$$

$$P_{nd} = P / \lambda U_{\infty} \quad (13)$$

Pressure and vorticity are common parameters for characterization of blade loading and energy exchange [2, 38, 46, 50]. Blade surface pressures are the source data for blade forces which were previously mentioned for angle of attack calculation (Equations 4-6). Vorticity is the curl of velocity, which often can be directly linked to pressure variations resulting from flow separation, as seen in the following figures.

Vortex shedding for the 120° foil is most significant for *Baseline* (Figure 27a). Likewise, the pressure coefficient at the trailing-edge for 120° (Figure 28a) is highly negative. A large trailing-edge vortex is attached to the foil in Figure 27a corresponding to the pressure difference at the blade surface, but it is mostly detached from the foil, and therefore not reflected in Figure 28a. In contrast, all pitch control cases seem to avoid the large pressure change at the trailing edge of the 120° foil. Another interesting result is observed for surface pressure of the 240° foil (Figure 28a). Though *Baseline* shows minimal pressure change, all cases increase the maximum pressure on the foil, which seems to have a net positive effect on downstream performance.

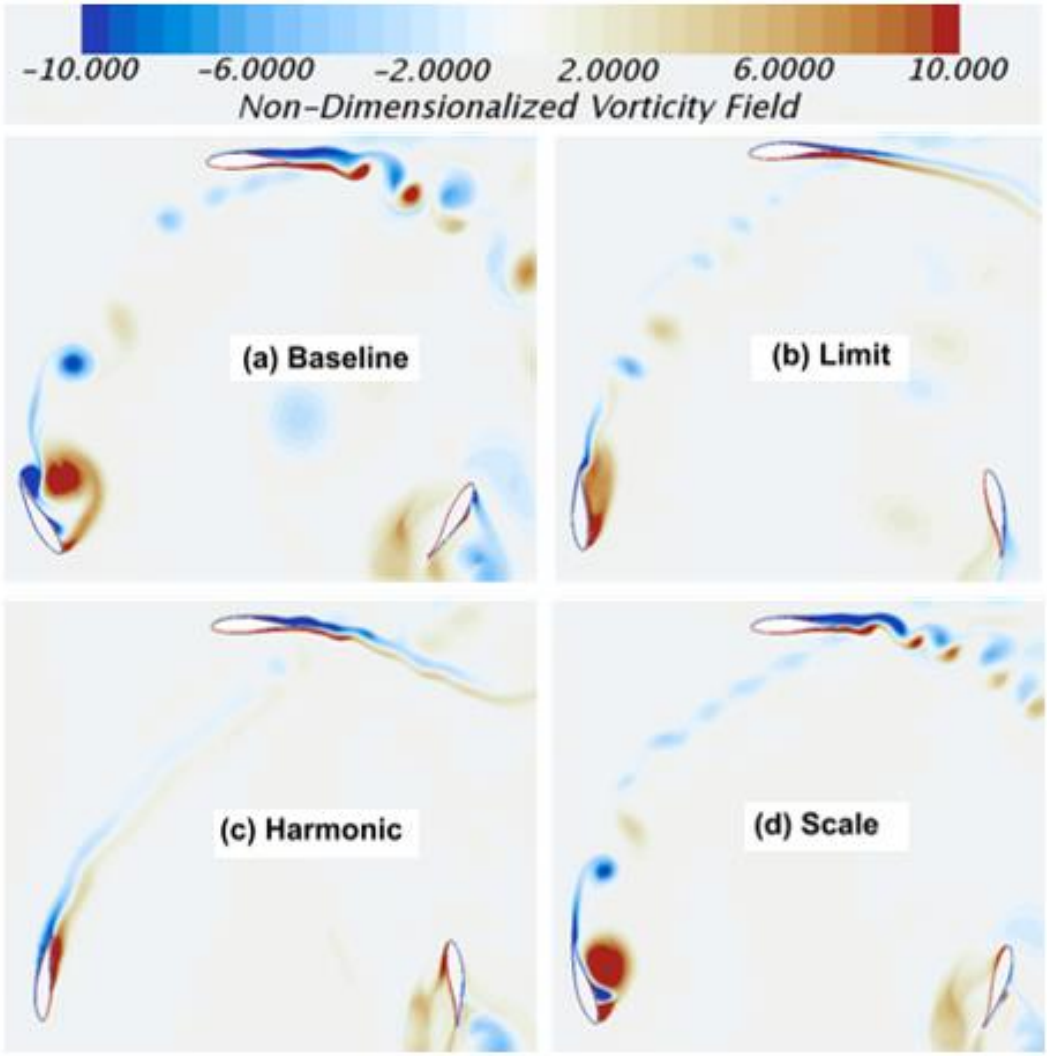

Figure 32. Vorticity for all cases, λ= 1.5

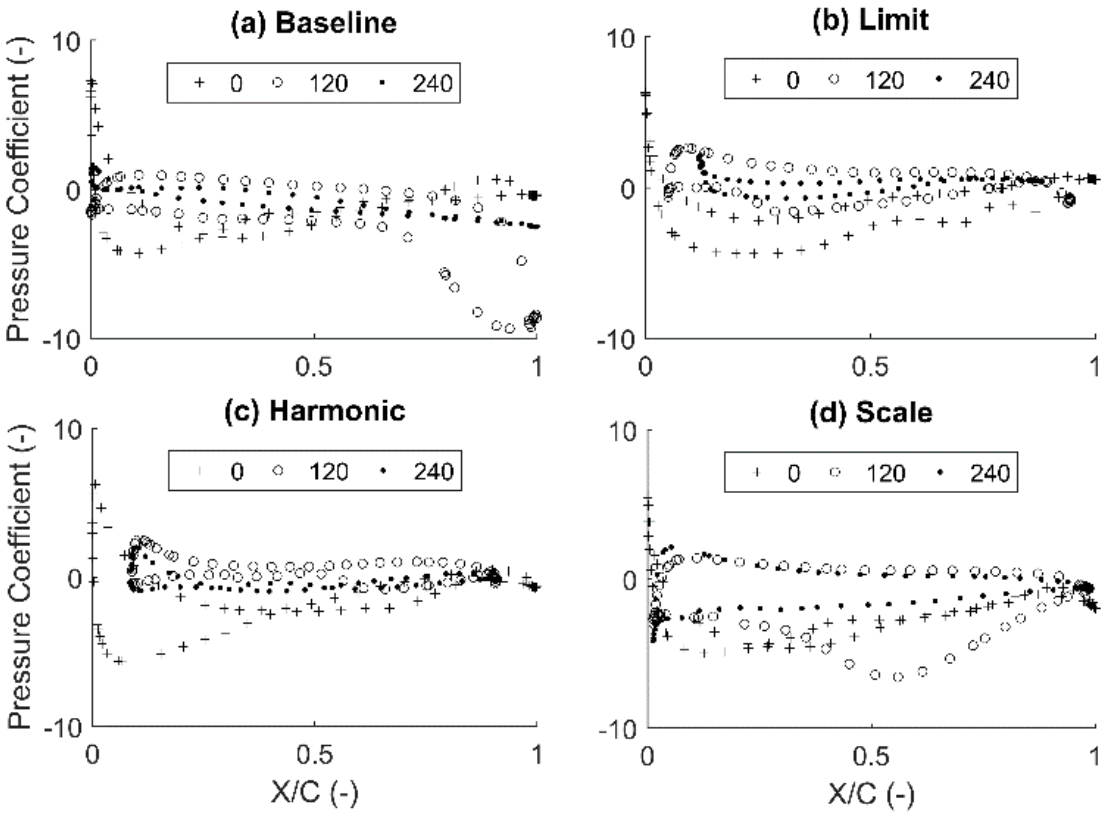

Figure 33. Surface pressure coefficient vs. chord position, λ= 1.5 (leading edge = 0)

Figures 34 and 35 show vorticity and pressure plots for all pitch cases compared to the *Baseline* case. The 120° *Baseline* foil (Figure 35a) has a large negative value that is indicative of the (red) leading-edge vortex in Figure 34a. *Limit* and *Harmonic* (Figures 35b and 35c) show negative pressure at their leading edge though only *Limit* has a visibly significant leading-edge vortex (Figure 34b). *Scale* has neither a leading-edge vortex nor negative pressure for the 120° foil (Figures 34d and 35d). The 240° location explains improved performance for *Harmonic* and *Scale* (Figures 35c and 35d) based on a completely positive pressure profile. In contrast, 240° *Limit* (Figure 35b) is almost completely in the negative pressure regime, explaining its inferior performance (Table 4).

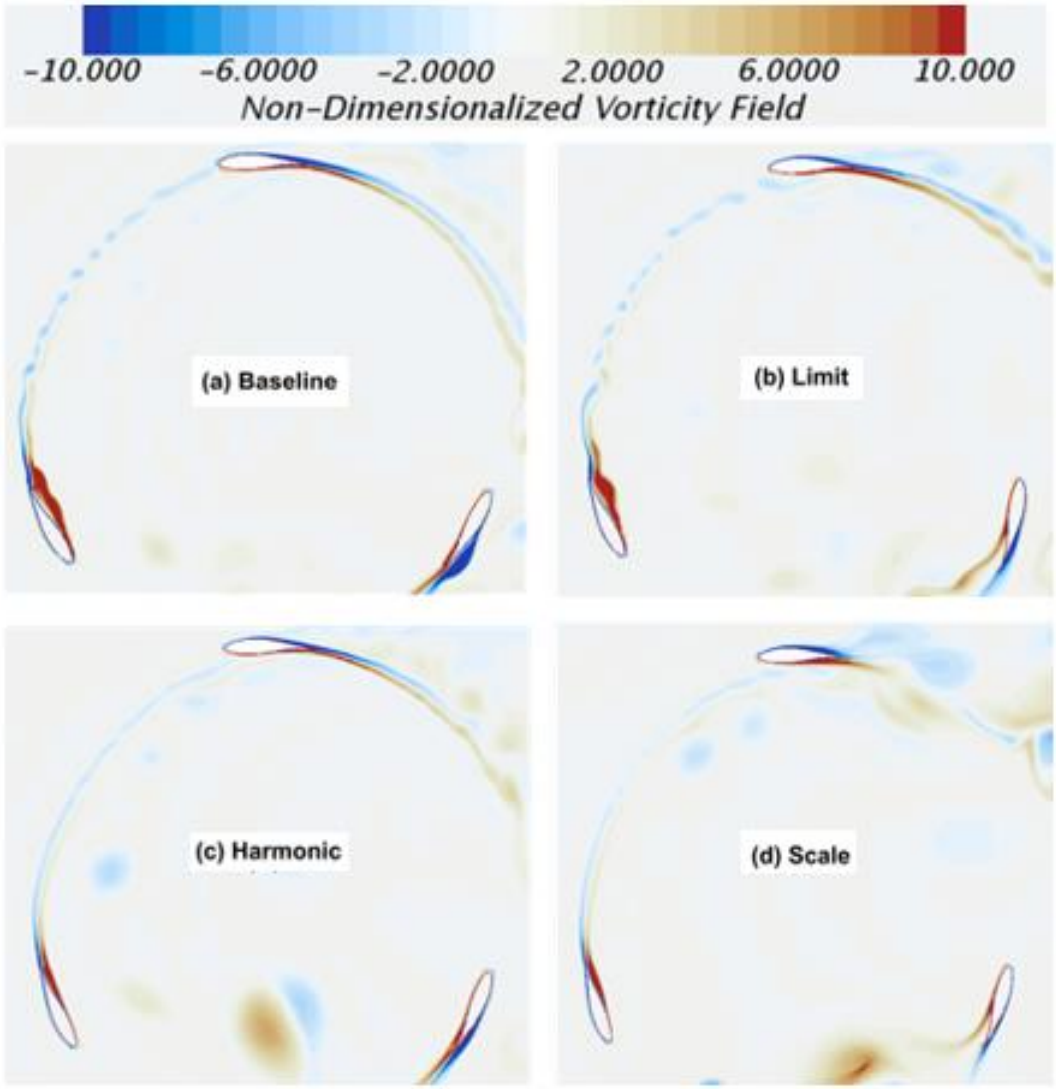

Figure 34: Vorticity for all cases, $\lambda = 3.0$

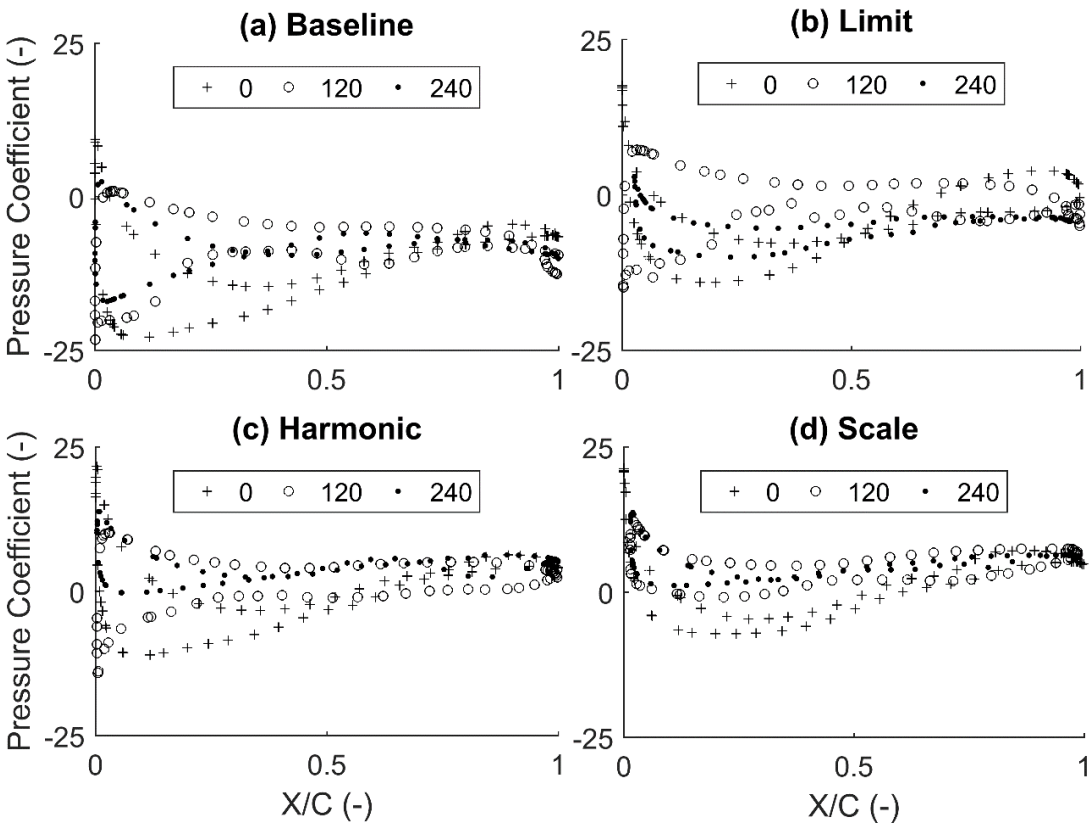

Figure 35: Surface pressure coefficient vs. chord position, λ= 3.0 (leading edge = 0)

Active Control

Amplification

Active control provides a litany of potential improvements upon system performance that passive control cannot. The focus of this study was to improve CFT operation based on the unknown relative blade velocities experienced in a constant input flow with insignificant turbulence. This preliminary study of active control utilizes only proportional gain in order to provide a foundational understanding of system response. Also, only $\lambda = 3.0$ is considered for all active results.

Figure 36 shows three active control results varying initial pitch βi along with a single passive control curve, with coefficient of performance (Cp) values for comparison. The straight line curves represent an initial βi of 0.5 which corresponds to a 10° angle of attack amplitude. Coefficient of performance values for the $\beta i = 0.5$ cases only differ by 0.002 Cp, suggesting passive and active controls are quite similar. Of the three active results, the highest Cp (0.600) is realized for an initial pitch value of 0.6 which is equivalent to a 12° angle of attack.

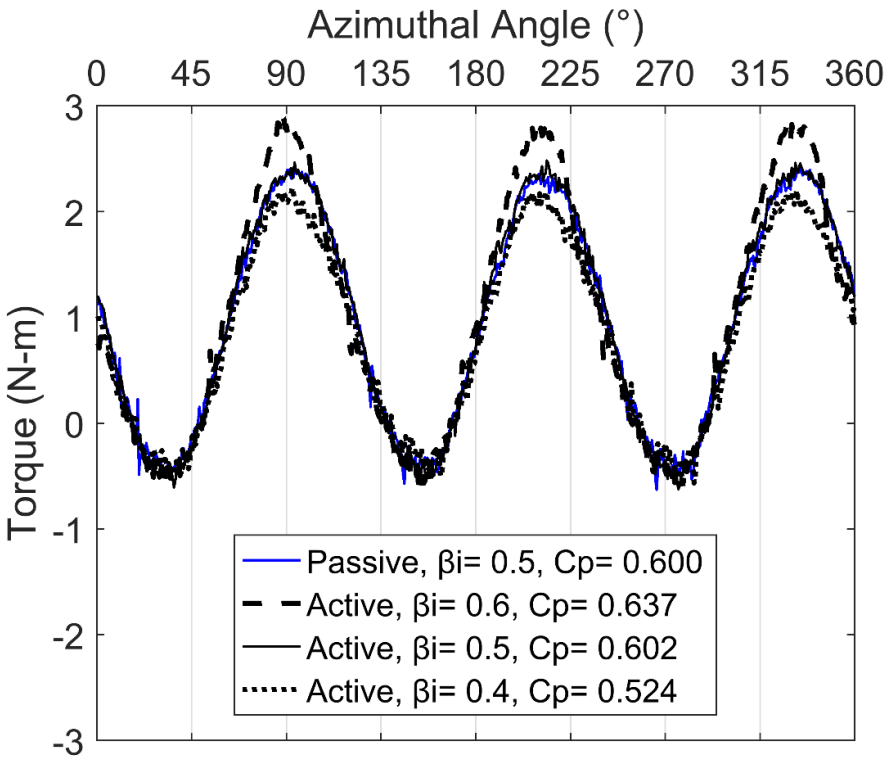

Figure 36: Total turbine torque, active control compared to passive (*Scale*)

Unlike Figure 36, Figure 37 shows a significant difference between the βi= 0.5 cases. Active control with βi= 0.5 has a minimum angle of attack that is 1.1° lower than passive control, suggesting that active control reduces the pitch requirement on the upstream side (0-180°) to account for unsteady flow effects. Predictably, the lowest angle of attack occurs for βi= 0.6 because it lessens the overall pitch requirement. Figures 36 and 37 are a good example of the relationship between performance and reliability; when coefficient of performance goes down, so does angle of attack which generally reduces thrust loading on the turbine.

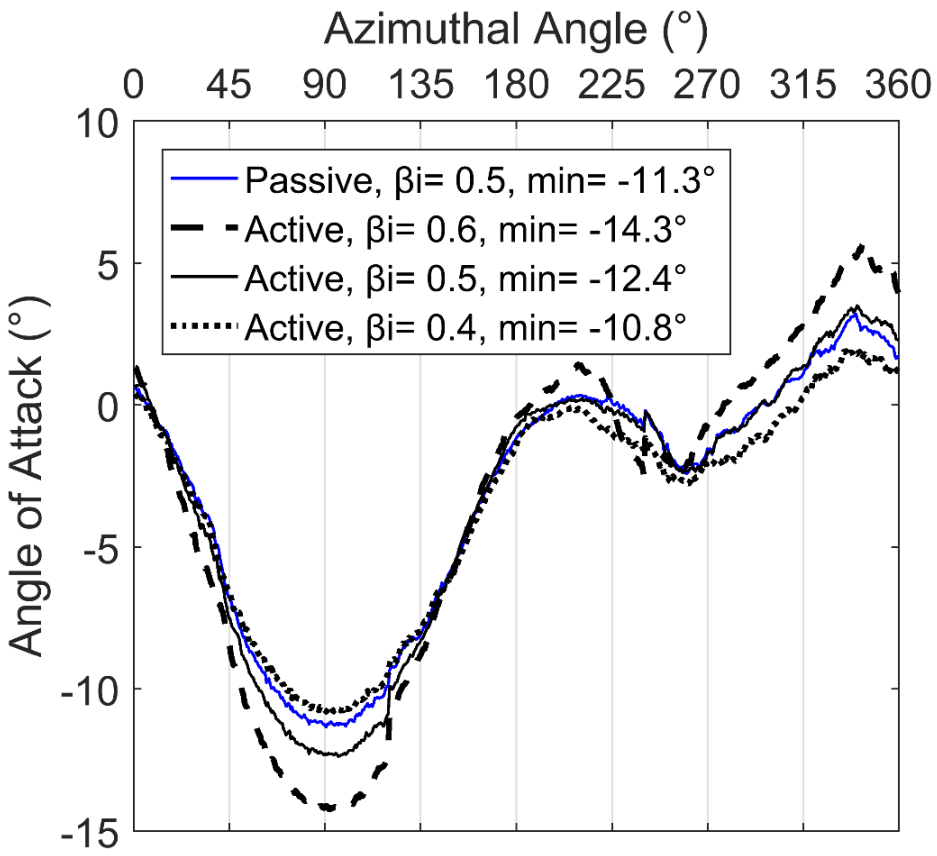

Figure 37: Instantaneous angle of attack

Figure 38 shows an individual blade's pitch rate profile for one revolution of the turbine, 0.314 seconds for λ= 3.0. Active control with βi= 0.5 makes a small difference, reducing rotation rate magnitude (7.03 rad/s) by only 4.4% relative to passive (βi= 0.5). Still, several observations can be made about active control: 1) peak rotation for all cases (around 180°) is shifted nearly 10° to the right of passive control, 2) rotation from 0-90° and 270-360° is flattened and even curved slightly upward in some cases, 3) acceleration of rotation rate magnitude for 90-180° is slightly smaller than deceleration (180-270°). Observation 1 is targeted in the next section (Phase Offset), where rotation is purposefully shifted to analyze the effect on system response. Observations 2 and 3 are relatively minor

but clearly depend on the error term (βe) as they are not represented by the passive result. As mentioned in Chapter 3, eliminating the ±0.2 βe limitation and/or the passive component of pitch βi should increase the effect of βe on the system.

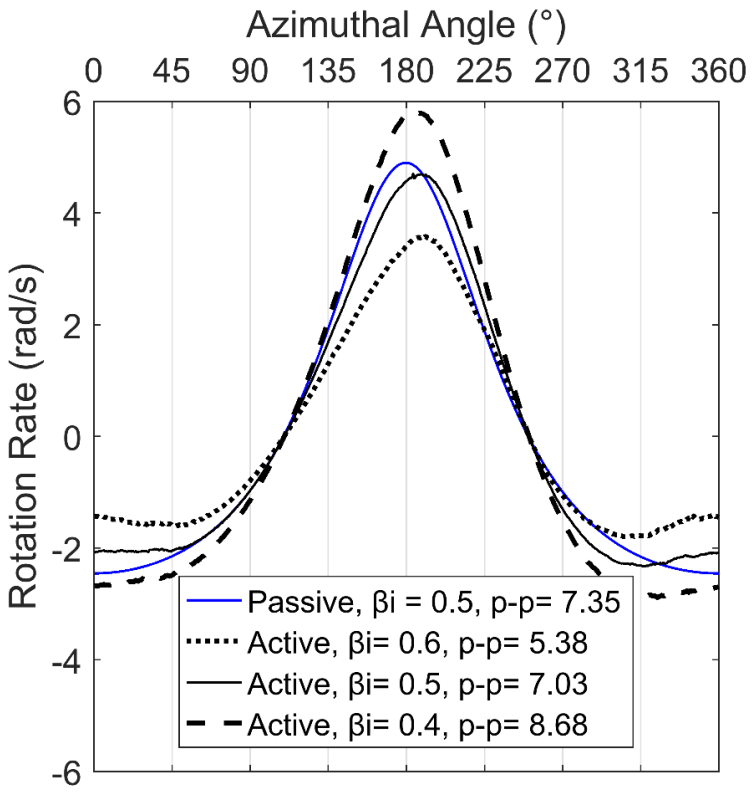

Figure 38: Individual blade pitch rate

Phase Offset

Passive pitch control simulation requires a choice of initial pitch angle and cannot adjust this setting once started. In contrast, active pitch control allows one the ability to directly vary the phase offset angle of the $\propto_n$ curve by shifting so that zero angle of attack occurs at a non-zero azimuthal angle. Figure 39 shows that the slope of the torque curve is significantly affected by relatively small changes in the $\propto_n$ set-point. The best

comparison can be made between 0° offset and 7.5° offset because their Cp values are nearly the same (0.601 vs. 0.596). The 0° offset shows a sharp drop at peak torque followed by a "shelf" for each blade; in contrast, the 7.5° offset does not exhibit the "shelf". Therefore, reliability gains may be achieved without a noticeable drop in performance.

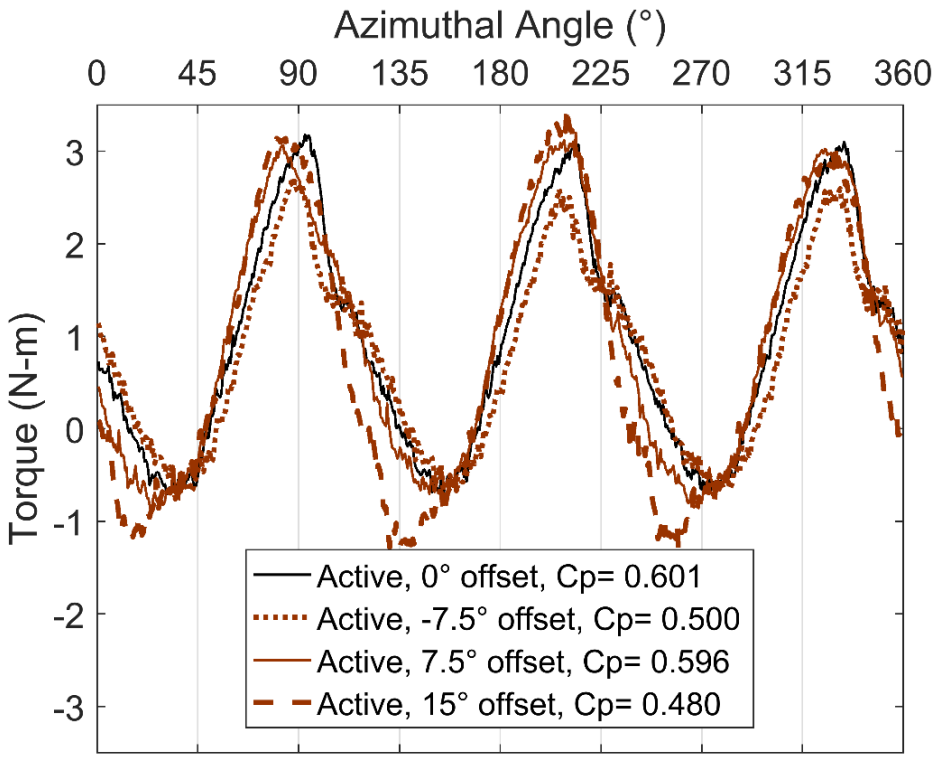

Figure 39: Total turbine torque, varying set-point phase offset

Figure 40 shows the instantaneous angle of attack curves for varying phase offset angles of the nominal set-point. As with the torque curve, a difference is noticed between the 0° and 7.5° offset angles, varying by 1.2° in minimum angle. However, 15° offset shows a peculiar result on the downstream (180-360°) side, where angle of attack settles at a negative angle of attack around 260° azimuthal angle which it maintains to the next

revolution (360°). In contrast, the -7.5° offset case maintains positive angle of attack values from about 1-11° within the same range. It seems that phase offset variation may have less of an effect on upstream angle of attack (the usual focus to improve performance) than on downstream angle of attack values. However, results at the 0° and 360° azimuthal angles are different enough to suggest that curves from only one revolution are inadequate to describe the simulations; this will be considered in future work.

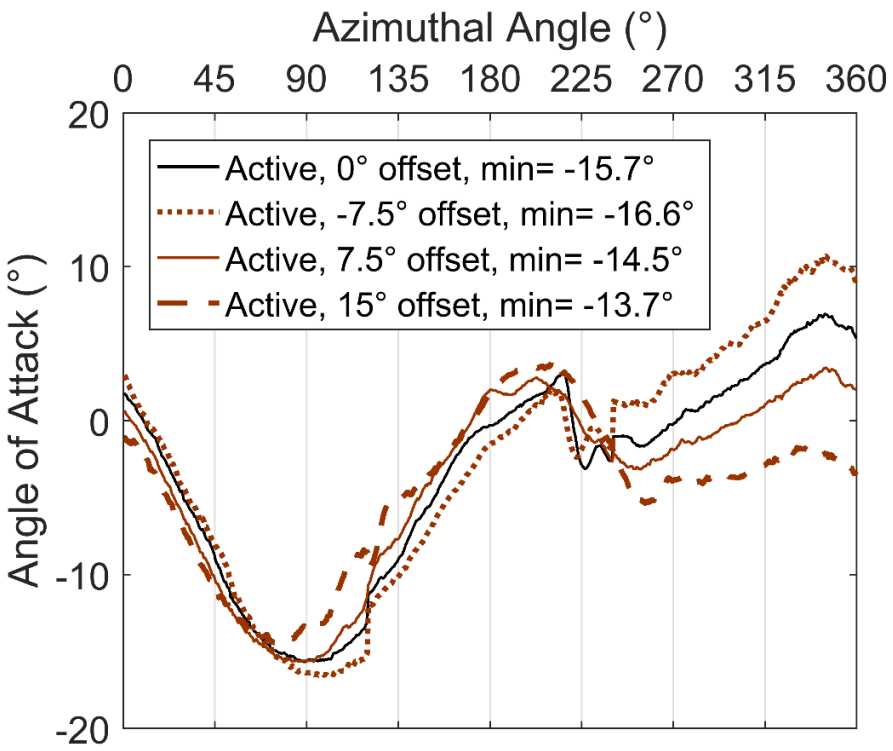

Figure 40: Instantaneous angle of attack, varying set-point phase offset

Figure 41 compares the blade rotation profiles for phase offset changes. Note that each case has the same initial pitch, so differences in the amount of rotation are purely due to the feedback control βe. As with Figures 39 and 40, Figure 41 shows the largest difference between -7.5° and 15° offset, with a 21% greater rotation rate for 15°. All of

the cases seem to obey the same basic profile; the largest difference comes for 15° where the pitch rate acceleration from 135° to 180° is considerably larger than the other cases. This echoes the slope variation in Figure 39 for turbine torque. Based on these results, it seems that phase-offsetting could help prove active control is a better option than passive.

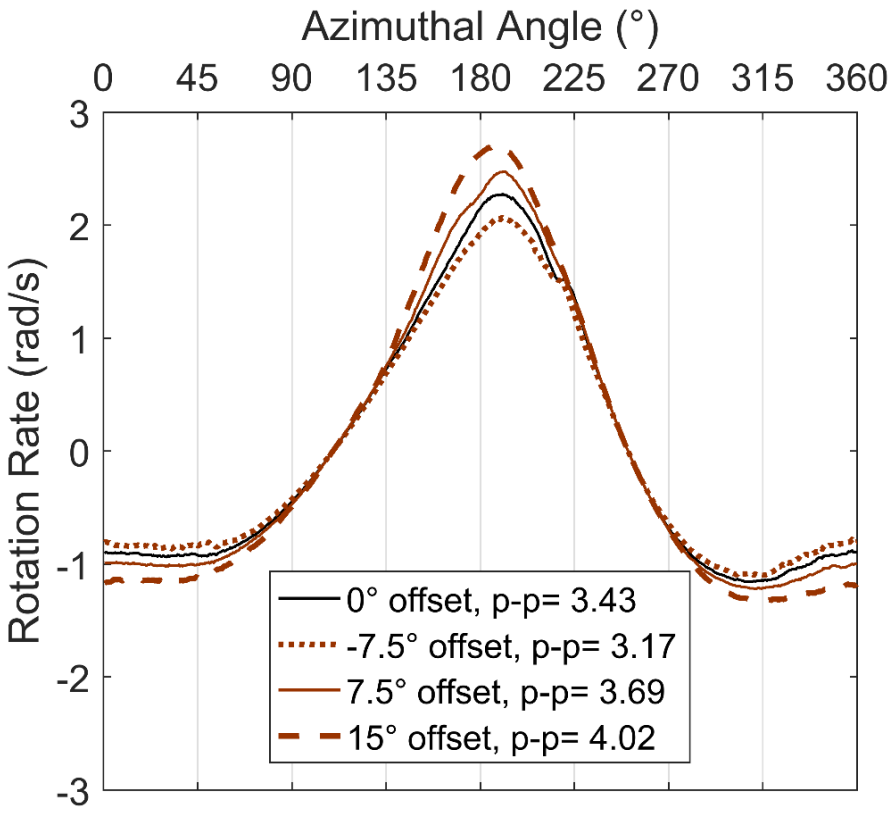

Figure 41: Individual blade pitch rate, varying set-point phase offset

CHAPTER FIVE

EXPERIMENTAL ANALYSIS

Past Work

In 2013, a CFT was initially designed and all of the components for fixed-pitch operation were selected [51]. Finite element analysis was conducted for the turbine rig structure, hub, and blades. Strain gage location was based off of Strickland's experiment, the same one used in this thesis [24], along with a Wheatstone bridge. Wheatstone bridges are commonly used with strain gages to get the correct values; the current setup is shown in Figure 42. R4 is the strain gage (350 Ω) which measures tensile strain, while R1 and R2 are half-bridge completion resistors. R3 completes the circuit ("dummy" resistor) and RL is the wire resistance, generally assumed to be zero. VEX is the input voltage from Arduino (5 volts) while VCH is the channel output that determines strain.

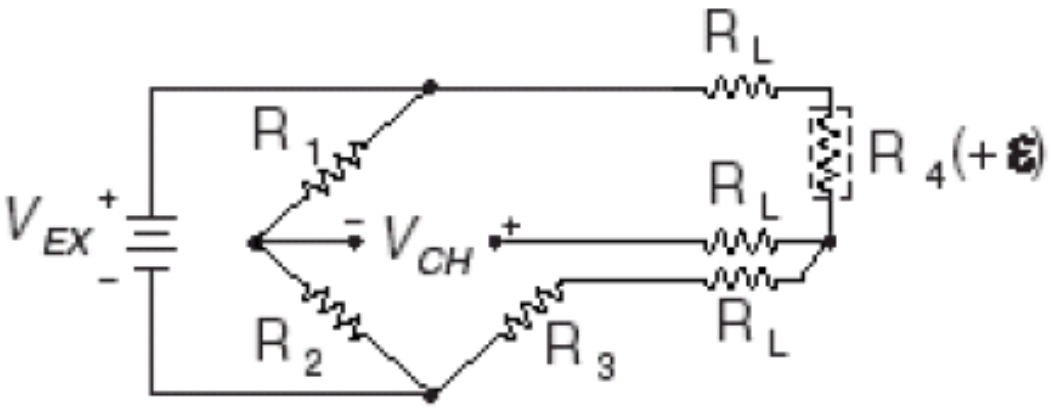

Figure 42: Wheatstone quarter-bridge circuit diagram (adapted from [52])

In 2015, there was a Capstone group that compiled many of the current turbine components [53]. The most essential of those components was the variable pitch hub (Figure 43) which features servo motors that linearly actuate to pitch each blade individually. As designed, each blade can vary from -6.06° to +12.6° [53]. Although the positive angle is about twice as high as the negative one, blades can be simply flipped 180 degrees so that the negative limit is larger. Arduino code was also written to drive each motor individually and as suggested by simulations. However, due to time limitations, only the fixed-pitch hub is tested in this thesis with the hope that findings will aide other students in variable-pitch preparation.

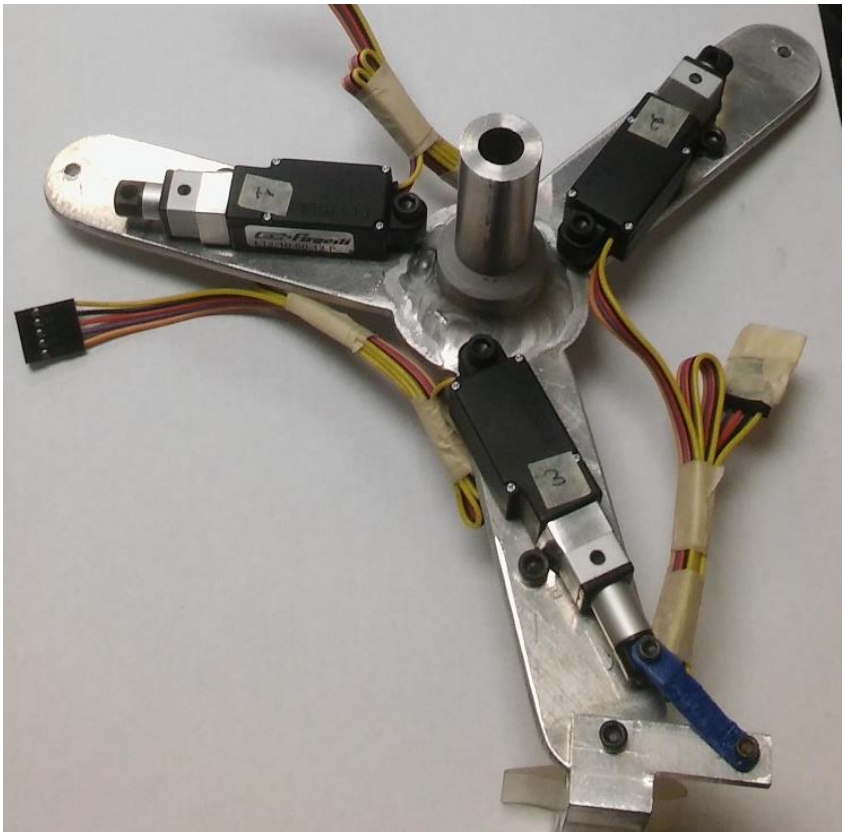

Figure 43: Variable pitch turbine hub with servo motors

Water Flume Characterization

To get an idea of the flow conditions the turbine might encounter experimentally, Acoustic Doppler Velocimetry (ADV) measurements were taken in November 2016. It was determined from those experiments that the average velocity of the flume is 0.72 m/s. In addition, turbulence intensity was measured but not incorporated into the simulation.

Turbulence intensity can be defined simply as the variation in velocity with time. Measurements were taken at multiple points between 15 and 30 feet downstream of the flume inlet to allow the flow to steady somewhat. Figures 44 and 45 show variation in velocity and turbulence intensity, respectively. The y- and z- velocities in Figure 44 seem to exhibit an oscillatory motion between 16 and 28 feet which can be attributed to the flume walls. However, the x-velocity in Figure 44 seems to disobey conservation of momentum as it actually speeds up considerably; the more likely explanation is that a decrease in flow height due to open channel flow causes a velocity increase. Figure 45 represents turbulence intensity, which is the root mean square velocity divided by the average velocity in three dimensions.

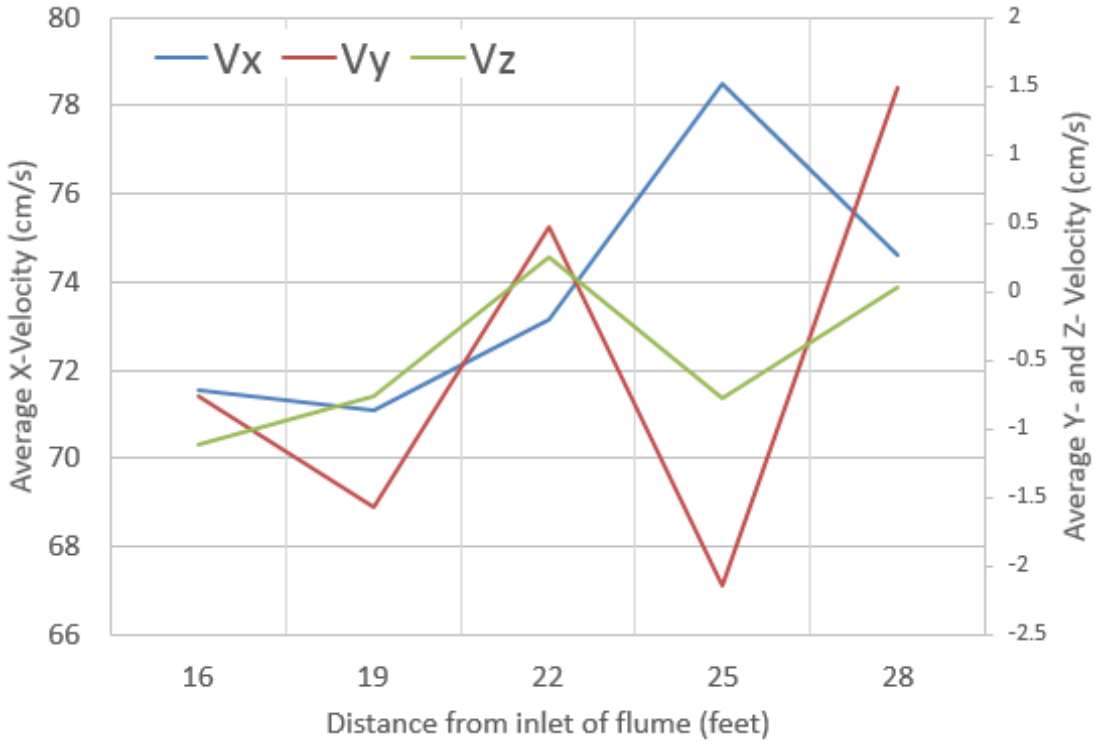

Figure 44: Water flume velocity in all directions (x is with current, y is transverse)

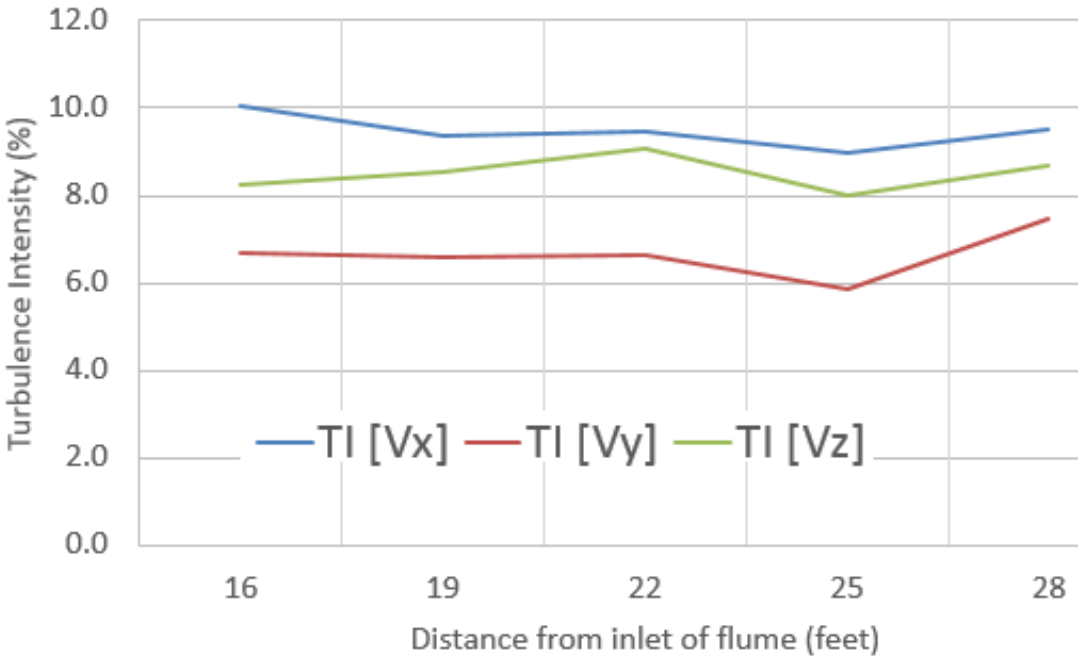

Figure 45: Turbulence intensity in all directions (x is with current, y is transverse)

Current Setup

The current setup with fixed-pitch linkages that connect the turbine hub and resin blades is shown in Figure 46a. In terms of measurement there is a limited number of cords that can be fit into the slip ring that keeps the cords from twisting around the rotor. However, a test with fixed blades has the benefit of no cords to the variable pitch motors on the hub. This will allow for more measurement of the turbine blades, which will be done using strain gage measurement (shown visually in Figure 46b) similar to the Texas Tech experiment [24]. Additionally, ADV measurement of the shed wake and dye injection will provide both quantitative and qualitative data while the turbine is tested. The degree of turbulence observed during the experiment will dictate where the turbine is placed along the thirty-foot expanse of the flume. Prior testing favored the second half of the flume, but this determination partially depends on the current flow rate at the flume inlet. A baffle may be considered at the inlet for faster flow diffusion.

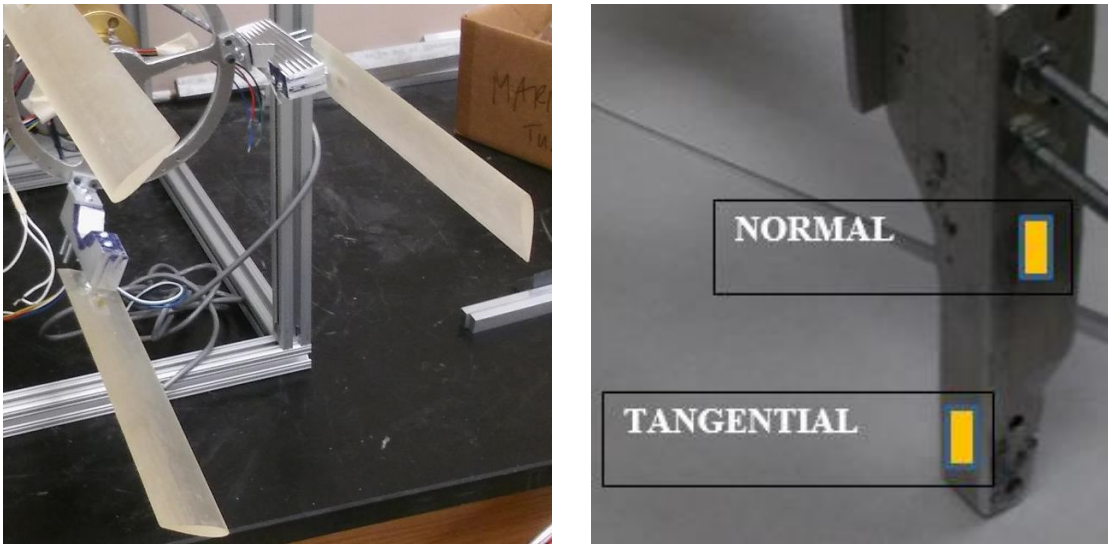

Figure 46: Experimental CFT: a) blade-hub assembly, b) strain gage locations

Experiment

The turbine rig with fixed-pitch NACA 0015 blades was tested on November 25th, 2017, for a continuous period of about thirty minutes. There were six different test cases, as seen in Table 7, varying three parameters: flow rate, output type (weir setup shown in Figure 47), and bottom slope of the flume. Five of the six cases both self-started and moved non-stop upon steady-state flow; the lone exception was with a full weir output that forced an input velocity of 0.163 m/s to prevent overflow, 23% of the design input velocity of 0.72 m/s. In general it was observed that the outlet weir had a significant effect on the water flow, while the effect of bottom slope was minimal. The fastest flow velocity, 1.05 m/s, resulted in a rotation rate of 14.5 rad/s or a tip-speed ratio of about 1.8. The $\lambda = 1.8$ value is on the low end of the simulated range (from $\lambda = 1.5$ to $\lambda = 3.0$). Although the physical results were promising, the strain gage measurements were not successfully recorded. Measurement recommendations along with guidelines for future experimentation will be covered at the end of this section.

Table 7: Experimental test cases

Case	*Rate (ft^3/s)*	*Output Type*	*Slope (in)*
1	1.94	Fully open	0.0
2	1.60	Small weir	0.0
3	0.70	Large weir	0.0
4	2.13	Fully open	-2.5
5	2.15	Small weir	-2.5
6	2.15	Small weir	-3.5

Figure 47: Full weir output with small metal weir clamped to flume

Test Cases

Table 7 gives all of the test cases covered during experimentation. As previously mentioned, Case 3 was the only non-spinning case due to a very small input velocity. Due to maximum flow limitations of the flume, the small weir output case gave the best results for rotation rate that correspond with simulations. The bottom slope of the thirty-foot-long flume was reduced slightly two separate times but did not have a significant effect on results. All six cases were tested at one stream-wise flume position, 15 ½ feet from the inlet, which gave a good representation of average flume conditions. Figure 48 shows the turbine rig looking in the downstream direction.

Figure 48: Turbine rig in flume test position

Measurements

All the simulations were conducted using two assumptions: 1) input velocity is constant, 2) tip-speed ratio is between 1.5 and 3.0 (i.e. the turbine rotates up to three times faster than the input velocity). However, the simulations do not consider mass of the turbine or inertial/drag forces encountered in the experimental case. Height of the water column was measured for three of the six cases so that input velocity could be deduced from volumetric flow rate (Table 7 above). Additionally, rotation rate was measured by a stopwatch for each case for tip-speed ratio calculation. Table 8 gives height, input velocity, tip-speed ratio, and angular velocity for each of the three cases.

Table 8: Experimental data for three of six test cases

Case	*Height (in)*	*Vin (m/s)*	*TSR (-)*	*ω (rad/s)*
1	7.0	0.676	0.92	5.76
2	10.5	0.558	1.17	6.07
5	6.0	0.874	1.79	14.50

Overall the test cases seem to be on the low end of the range for tip-speed ratio, particularly Case 1 which has a tip-speed ratio less than 1 (0.92). However, both height and input velocity were measured at the flume inlet, so they may vary from what the turbine experienced. Case 2 has a lower velocity input than Case 1, but the water column height is much greater due to the small weir at the flume outlet. Thus, Case 2 has a tip-speed ratio larger than one (1.17). The only case that has a tip-speed ratio within the simulation range is Case 5 with a value of 1.79. Though Case 5 had the lowest inlet water height, its velocity input was much greater than that of the other two cases in Table

8. Without the Arduino data it is unclear what the torque values are which are necessary to calculate coefficient of power; however, it is inferred that friction losses due to the rotor and drivetrain (not captured by simulation) may cause lower tip-speed ratios.

Figure 49: Experimental blade deflection: a) blade at 90°, b) blade at 270°

Extrema for blade deflection (y) of the turbine in Case 5 are shown in Figure 49. As expected, the upstream (90°) condition shows the highest value, 1.14 inches (0.029 m) or 10.8°. The downstream position, 270°, is 0.28 inches (0.007 m) or about 25% of upstream. If each blade is assumed to be a cantilever beam, these deformation values can be converted to normal force which can be converted to angle of attack and compared to simulated values. Stratasys, owners of the Polyjet product line for 3D printers, gives the maximum modulus of elasticity for ABS plastics as 3.0 GPa [54]. The cantilever beam equation for deformation is re-arranged to find normal forces; see Appendix B for calculation details.

Instantaneous angle of attack can be estimated at both the upstream and downstream positions using aforementioned equations to convert normal force. An assumption needs to be made for tangential force in order to complete the calculation; in this case, tangential force is considered an order of magnitude smaller than normal force, so that FN = 84 N and FT = 8.4 N. The result is an instantaneous angle of attack equal to about -19°, nearly 30% smaller than the simulated value at the 90° azimuth for a tip-speed ratio of 2.0 (Chapter 4). One possible reason for this difference is that the blades may not be at zero angle of attack to begin with; another is the tip-speed ratio difference (1.79 vs. 2.0). In contrast, the tangential force value of 4.5° is slightly higher than the simulated value around 4.0° (Chapter 4). It was also discovered after the experiment that two of the three blades are slightly bent to begin with, so future testing should include marking the blades so that the zero value can be subtracted from the measured values.

Qualitative Results

With the flow direction from left to right, Figure 50 shows the beginning of vortex build-up on the left-most blade. Figure 50a shows the blade bending significantly toward the low pressure created by the flow structure, while Figure 50b clearly shows rotational flow behind the blade.

Figure 50: Leading edge vortex (LEV) builds up: a) blade at 90°, b) blade at 120°

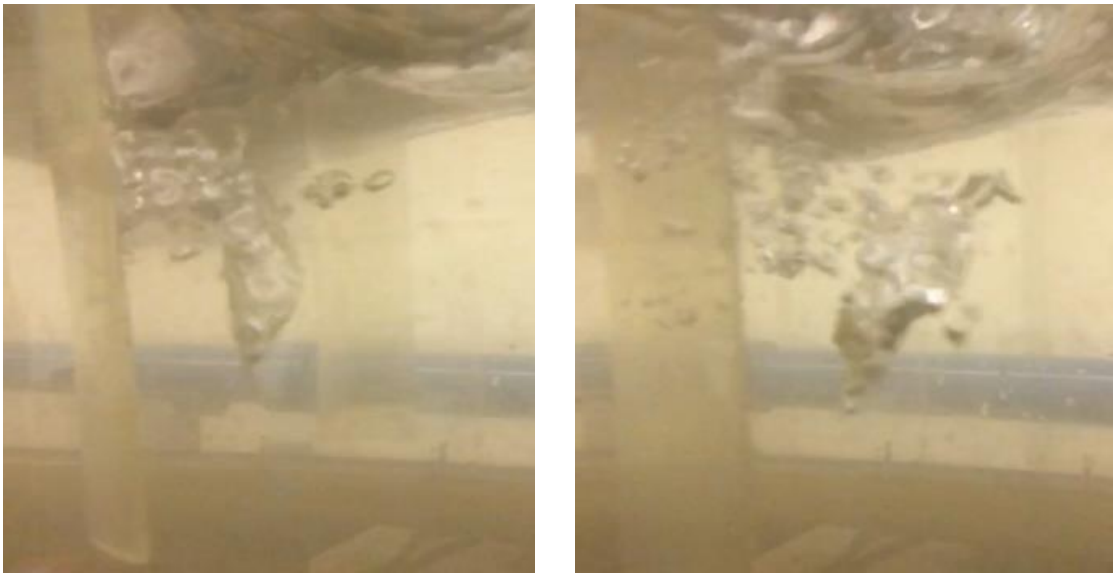

Figure 51: LEV sheds into turbine wake: a) blade at 150°, b) blade at 180°

Figure 51a gives a good visualization of the vortex in the process of shedding from the blade. While RANS simulation only produces averaging of the bulk flow, there are clearly quite a few smaller turbulent eddies shedding from the blade particularly in Figure 51b. That being said, a strong vortex is clearly shed (center of Figure 51b) which is reflected well by the RANS simulation *Baseline* (Figure 52).

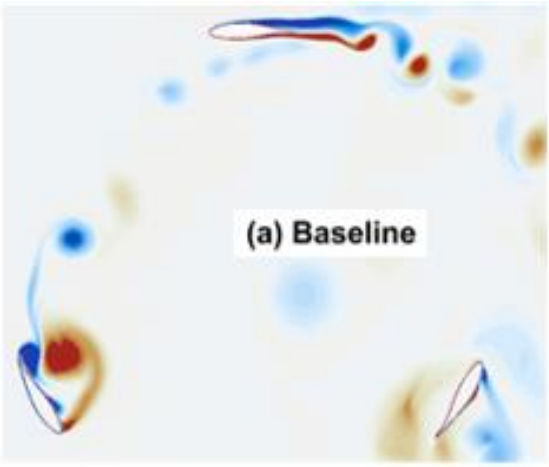

Figure 52. *Baseline* vorticity, $\lambda = 1.5$

Dye injection can be seen in Figure 53, done with food coloring upstream of the turbine. However, this did not provide any improvement to speak of with flow visualization. Other researchers have attached dye injectors to the tip of blades to better show tip vortices. This method (among others) must be considered if dye injection is to be useful.

Figure 53: Dye injection (blue) in center of flume

Future Recommendations

Measurement by optical encoder and strain gages (Arduino) must be further investigated so that they are functional during future tests. If necessary, LabView may be considered as an alternative to Arduino. Also, only NACA 0015 blades were tested, but the MHK F1-180 blade type was the only one simulated with RANS. For apples-to-apples comparison future experiments should certainly incorporate the MHK type blades. This fixed-pitch experiment was valuable to ensure that the rig and rotor are well-equipped for testing with any hub, and identified that both the Arduino and dye injector should be better understood before further experiments takes place.

CHAPTER SIX

CONCLUSION

Hydrokinetic turbine technology has the potential to be a significant source of renewable energy, particularly in areas of the world where land area for wind turbines is limited or non-existent. This work suggests that passive pitch control can drastically increase Lifetime Energy Capture (up to 149%) of the cross-flow turbine while at the same time reduce Operations and Maintenance Cost (135% thrust reduction). Taken together, these percentages imply a potential 201% increase in Cost of Energy. However, passive control is motivated primarily by the desire to control upstream angle of attack, therefore the downstream flow is not optimized. Active control, on the other hand, allows for multiple parameters to be considered at once based on adjustment to real-time flow conditions including dynamic stall and wake velocity deficit.

Future simulation work should consider both passive and active control. The experiment featured variable inflow velocities while all simulations only used one velocity value; further passive control simulations should consider these different inflows, and perhaps even the turbulence intensity measured by the ADV. Active control simulation suffered in the thesis because only a tip-speed ratio of three was tested, which does not see significant dynamic stall effects. Further work is underway currently to test low tip-speed ratios where active control may be the most effective. Optimization of the cross-flow turbine in the research and design phase is essential if the technology is to be implemented for large-scale electricity generation.

REFERENCES CITED

1. Muljadi, E. and Y.-H. Yu, *Review of Marine Hydrokinetic Power Generation and Power Plant.* Electric Power Components and Systems, 2015. **43**(12): p. 1422-1433.

2. Ferreira, C., *The near wake of the VAWT: 2D and 3D views of the VAWT aerodynamics*. 2009, TU Delft, Ph.D. thesis.

3. *Ocean currents image*. Available from: https://media1.britannica.com/eb-media/57/70057-004-85830DA6.jpg.

4. Energy, N. *Community Works: 2017 Report*. 2017; Available from: http://www.northwesternenergy.com/docs/default-source/documents/community/community_report.pdf.

5. Johnson, S.J., van Dam, C.P., Berg, D.E., *Active Load Control Techniques for Wind Turbines*. 2008: Sandia National Laboratories.

6. Kirke, B.K. and L. Lazauskas, *Limitations of fixed pitch Darrieus hydrokinetic turbines and the challenge of variable pitch.* Renewable Energy, 2011. **36**(3): p. 893-897.

7. Gorle, J.M.R. *Critical Analysis of the Effectiveness of Blade Pitching for Vertical Axis Water Turbine*. in *European Wave and Tidal Conference, Nantes, France*. 2015.

8. Strom, B. *Consequences of Preset Pitch Angle on Cross-Flow Turbine Hydrodynamics*. in *EWTEC*. 2015.

9. U.S. Energy Information Administration. *Annual Energy Outlook with projections to 2050*. 2017; Available from: http://www.eia.gov/outlooks/aeo/pdf/0383(2017).pdf.

10. Ocean Renewable Energy Group. *Bay of Fundy tidal-power turbines clear first hurdle*. June 2008; Available from: http://www.oreg.ca/bi-weekly.html?subaction=showfull&id=1212619925&archive=&start_from=&ucat=1&.

11. Puget Sound Tidal Energy Web Site. *Proposed Tidal Energy Projects Located in Puget Sound*. October 2008; Available from: http://www.pstidalenergy.org/projects.htm.

12. Wind and Hydropower Technologies, *Feasibility Assessment of the Water Energy Resources of the United States for New Low Power and Small Hydro Classes of Hydroelectric Plants*, US Department of Energy Energy Efficiency and Renewable Energy, Editor. January 2006, Report: DOE-ID-11263.

13. Khan, M.J., et al., *Hydrokinetic energy conversion systems and assessment of horizontal and vertical axis turbines for river and tidal applications: A technology status review.* Applied Energy, 2009. **86**(10): p. 1823-1835.

14. Peebles, G., *Bathymetric effects on marine hydrokinetic array performance*. Masters thesis 2015, Montana State University.

15. Burton, T., Jenkins, N., Sharpe, D., Bossanyi, E., *Wind Energy Handbook*. 2nd ed. 2011: John Wiley & Sons.

16. *Darrieus Turbine image*. Available from: http://www.wind-works.org/cms/typo3temp/pics/Alcoa-VAWT-Newport-Oregon-1982_c57a57ab03.jpg.

17. *HAWT image*. Available from: http://citris-uc.org/wp-content/uploads/2013/12/wind_turbine_Intermittency-friendly_super-efficient_tri-gen-1013x580.jpg.

18. Choudhry, A., et al., *An insight into the dynamic stall lift characteristics.* Experimental Thermal and Fluid Science, 2014. **58**: p. 188-208.

19. Salter, S.H., *Are Nearly all Tidal Stream Turbine Designs Wrong?* 4th International Conference on Ocean Energy, 2012.

20. Wind Turbines - Betz Law Explained. 2010; Available from: http://c21.phas.ubc.ca/article/wind-turbines-betz-law-explained.

21. Klimas, P.C., *Darrieus Rotor Aerodynamics*, Sandia National Laboratories Transactions of the ASME, Editor. 1982, Vol: 104, pp. 102-105.

22. Laneville, A., *Dynamic Stall: The Case of the Vertical Axis Wind Turbine.* Journal of Solar Energy Engineering, Transactions of the ASME, 1986. **Vol 108**: p. 140-145.

23. Migliore, P.G., *Flow Curvature Effects on Darrieus Turbine Blade Aerodynamics.* Journal of Energy, 1980. **4**(2): p. 49-55.

24. Strickland, J.H., Smith, T., Sun, K., *A Vortex Model of the Darrieus Turbine: an Analytical and Experimental Study*. 1981: Texas Tech University, Prepared for Sandia National Laboratories under Contract No 06-4178.

25. Veers, P.S., *Blade Fatigue Life Assessment with Applications to VAWTs.* Solar Energy Engineering, 1982. **104**(106-111).

26. Hwang, I.S., Y.H. Lee, and S.J. Kim, *Optimization of cycloidal water turbine and the performance improvement by individual blade control.* Applied Energy, 2009. **86**(9): p. 1532-1540.

27. Maître, T., E. Amet, and C. Pellone, *Modeling of the flow in a Darrieus water turbine: Wall grid refinement analysis and comparison with experiments.* Renewable Energy, 2013. **51**: p. 497-512.

28. Belhache, M., Grangeret, P., Mouaze, D., Guillou, S., J-R Angielella,, *On the energy potential associated with blades radial force in a Marine Vertical Axis Turbine: performance optimization by a numerical study.* European Wave and Tidal Energy Conference, 2015.

29. Zeiner-Gundersen, D.H., *A novel flexible foil vertical axis turbine for river, ocean, and tidal applications.* Applied Energy, 2015. **151**: p. 60-66.

30. Paraschivoiu, I., *Wind Turbine Design: With Emphasis on Darrieus Concept*. 2002: Presses inter Polytechnique.

31. Shiu, H., van Dam, C., Johnson, E., et al., *A Design of a Hydrofoil Family for Current-Driven Marine-Hydrokinetic Turbines.* ASME, 2012.

32. Leishman, J.G., *Challenges in Modelling the Unsteady Aerodynamics of Wind Turbines.* Wind Energy, 2002. **5**: p. 85-132.

33. Leishman, J.G., *Principles of helicopter aerodynamics*. Cambridge Aerospace Series. 2000: Cambridge Aerospace Series.

34. Sheng, W., Galbraith, R. A. McD., Coton, F.N., *A new stall onset criterion for low speed dynamic stall.* Journal of Solar Energy Engineering, 2006. **128**(4): p. 461-471.

35. Bianchi, F.D., Battista, H.D., Mantz, R.J., *Wind Turbine Control Systems: Principles, Modelling and Gain Scheduling Design*, ed. S.-V.L. Limited. 2007.

36. Bossanyi, E.A., P.A. Fleming, and A.D. Wright, *Validation of Individual Pitch Control by Field Tests on Two- and Three-Bladed Wind Turbines.* IEEE Transactions on Control Systems Technology, 2013. **21**(4): p. 1067-1078.

37. Lazauskas, L., *Three Pitch Control Systems for Vertical Axis Wind Turbines Compared.* Wind Engineering, 1992.

38. Paillard, B., J.A. Astolfi, and F. Hauville, *URANSE simulation of an active variable-pitch cross-flow Darrieus tidal turbine: Sinusoidal pitch function investigation.* International Journal of Marine Energy, 2015. **11**: p. 9-26.

39. Vandenberghe, D., Dick, E., *A Theoretical and Experimental Investigation into the Straight Bladed Vertical Axis Wind Turbine with Second Order Harmonic Pitch Control.* Wind Engineering, 1986. **10**(3): p. 122-138.

40. Lazauskas, L., Kirke, B.K., *Modeling passive variable pitch cross flow hydrokinetic turbines to maximize performance and smooth operation.* Renewable Energy, 2012.

41. Pope, S.B., *Turbulent Flows*. 2000: Cambridge University Press.

42. Wilcox, D.C., *Turbulence Modeling for CFD*. 3rd ed. 2006.

43. Suluksna, K., Juntasaro, E., *Correlations for modeling transitional boundary layers under influences of freestream turbulence and pressure gradient.* International Journal of Heat and Fluid Flow, 2009. **30**(1): p. 66-75.

44. White, F.M., *Viscous Fluid Flow*. Third ed. 2006: McGraw Hill.

45. Drela, M. *XFOIL User Manual*. Available from: http://web.mit.edu/drela/Public/web/xfoil/.

46. Katz, J., Plotkin, A., *Low-Speed Aerodynamics: From Wing Theory to Panel Methods*. 1991: McGraw Hill, United States of America.

47. Staelens, Y., Saeed, F.F., Paraschivoiu, I., *A Straight-Bladed Variable-Pitch Concept for Improved Power Generation.* ASME Wind Energy Symposium, 2003: p. 146-154.

48. Bennett, S., *A Brief History of Automated Controls.* IEEE Control Systems, 1996.

49. Wescott, T., *PID without a PhD.* EE Times-India, 2000.

50. Ferreira, C., Scheurich, F., *Demonstrating that power and instantaneous loads are decoupled in a vertical-axis wind turbine.* Wind Energy, 2014. **17**: p. 385-396.

51. Logan, C., Jobst, T., Albares, Scott, *Capstone Project: Crossflow Turbine Research Test Rig.* 2013.

52. Transducer Techniques. *Quarter Bridge, Half Bridge and Full Wheatstone Bridge Strain Gauge Load Cell configurations,*. Available from: https://www.transducertechniques.com/wheatstone-bridge.aspx.

53. Luoma, J., Paschke, B.,, *EMEC 499R Capstone: Mechanical Engineering Design II.* 2015.

54. *Modulus of elasticity for ABS plastics*. Available from: http://www.stratasys.com/materials/polyjet/digital-abs.

APPENDICES

APPENDIX A

FORCE ESTIMATION WITH XFOIL-MATLAB

Sinusoidal pitching as outlined in this work is rooted in a 1992 study by Lazauskas who desired to lessen blade angle of attack (i.e. “feather” the blade) [37]. Twenty years later, in 2012, he introduced another study which predicts a peak efficiency about 50% greater with variable pitch along with two-to-three times less shaking force on the turbine [40]. In the 2012 paper, Lazauskas shows the ability to predict performance without considering dynamic stall.

A similar attempt was made in MATLAB by interpolating lift and drag force data from XFOIL static stall curves based on the nominal angle of attack predicted for both the *Baseline* and *Scale* cases. As described earlier, lift and drag can be converted to instantaneous angle of attack for CFT performance prediction, and MATLAB provides a low-order model that reduces solution time from hours (with CFD) to minutes. Ultimately this effort did not provide enough accuracy to be particularly useful. However, it can be generally observed that better agreement occurs between CFD and MATLAB when analyzing *Scale* (Figures A4-A6) than *Baseline* (Figures A1-A3), since *Scale* has lower angles of attack which are better represented by the XFOIL curves.

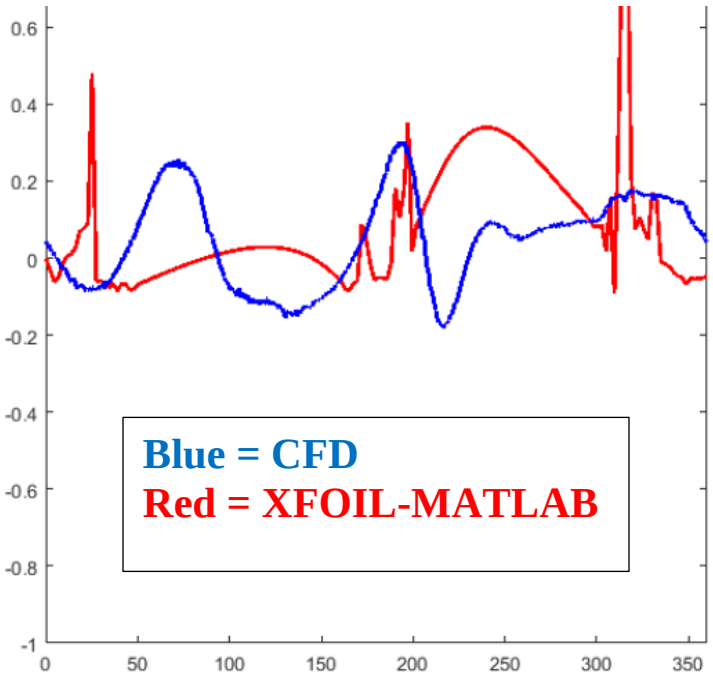

Figure A1: Tangential coefficient vs. azimuthal angle, *Baseline*, λ= 2.0

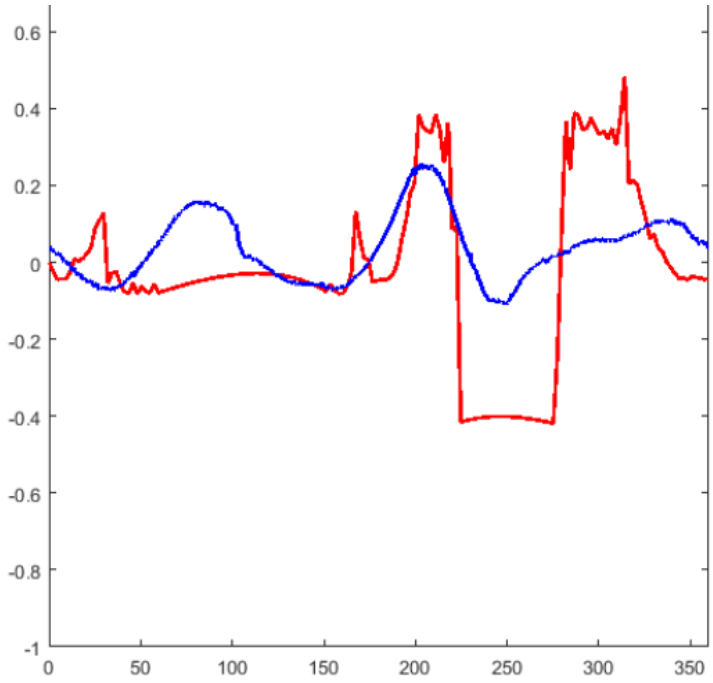

Figure A2: Tangential coefficient vs. azimuthal angle, *Baseline*, λ= 2.5

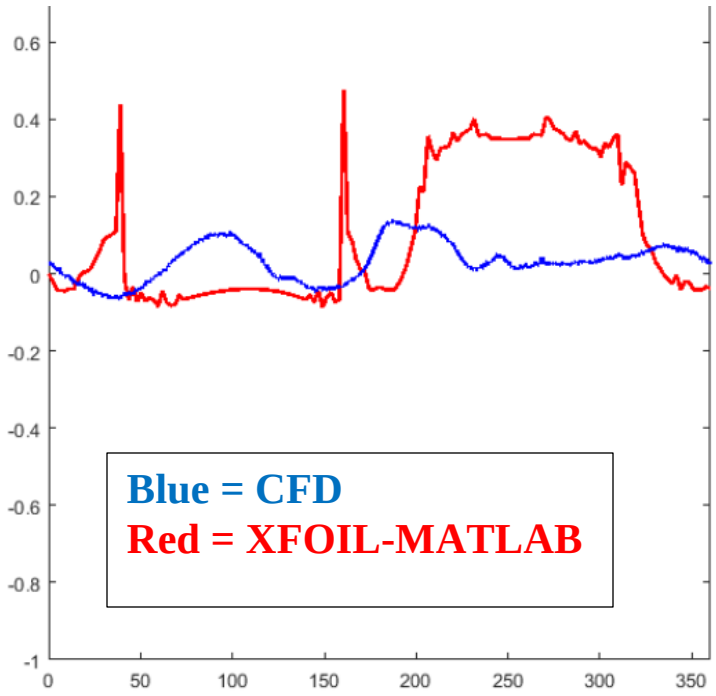

Figure A3: Tangential coefficient vs. azimuthal angle, *Baseline*, λ= 3.0

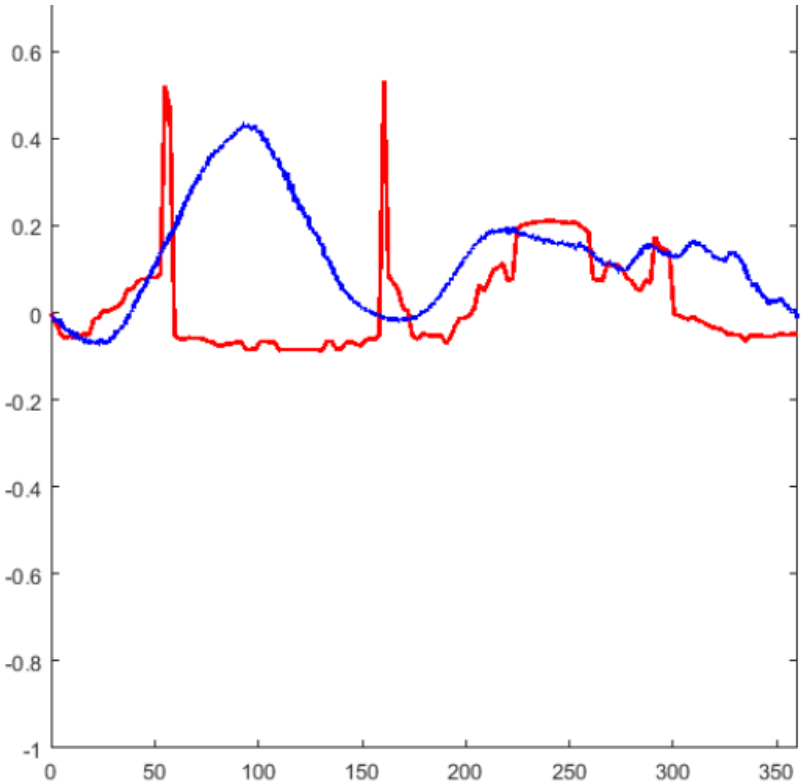

Figure A4: Tangential coefficient vs. azimuthal angle, *Scale*, λ= 2.0

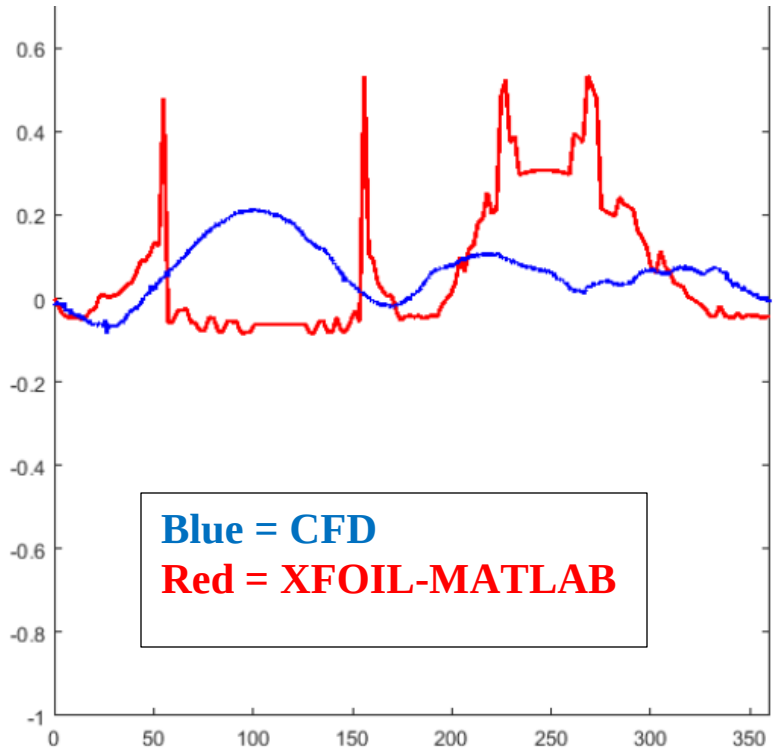

Figure A5: Tangential coefficient vs. azimuthal angle, *Scale*, λ= 2.5

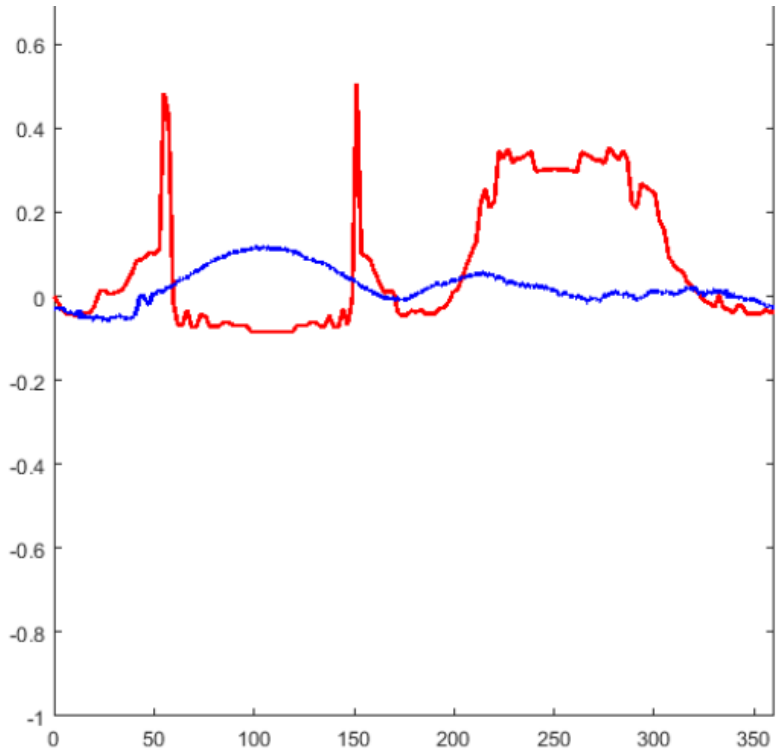

Figure A6: Tangential coefficient vs. azimuthal angle, *Scale*, λ= 3.0

APPENDIX B

HYDRODYNAMIC FORCE CALCULATION

Figure B1 gives the calculation method. Moment of inertia is estimated as a rectangular beam 1.5 inches long by 0.225 inches thick (maximum thickness of the NACA 0015 blade). Length of the blade is 10 inches and height of the water column is 6 inches. With these values, the maximum blade deformation (90° case) indicate a normal force of about 84 Newtons. This 270° case is much smaller, only about 20 Newtons, which is representative of the large wake deficit associated with low tip-speed ratios.

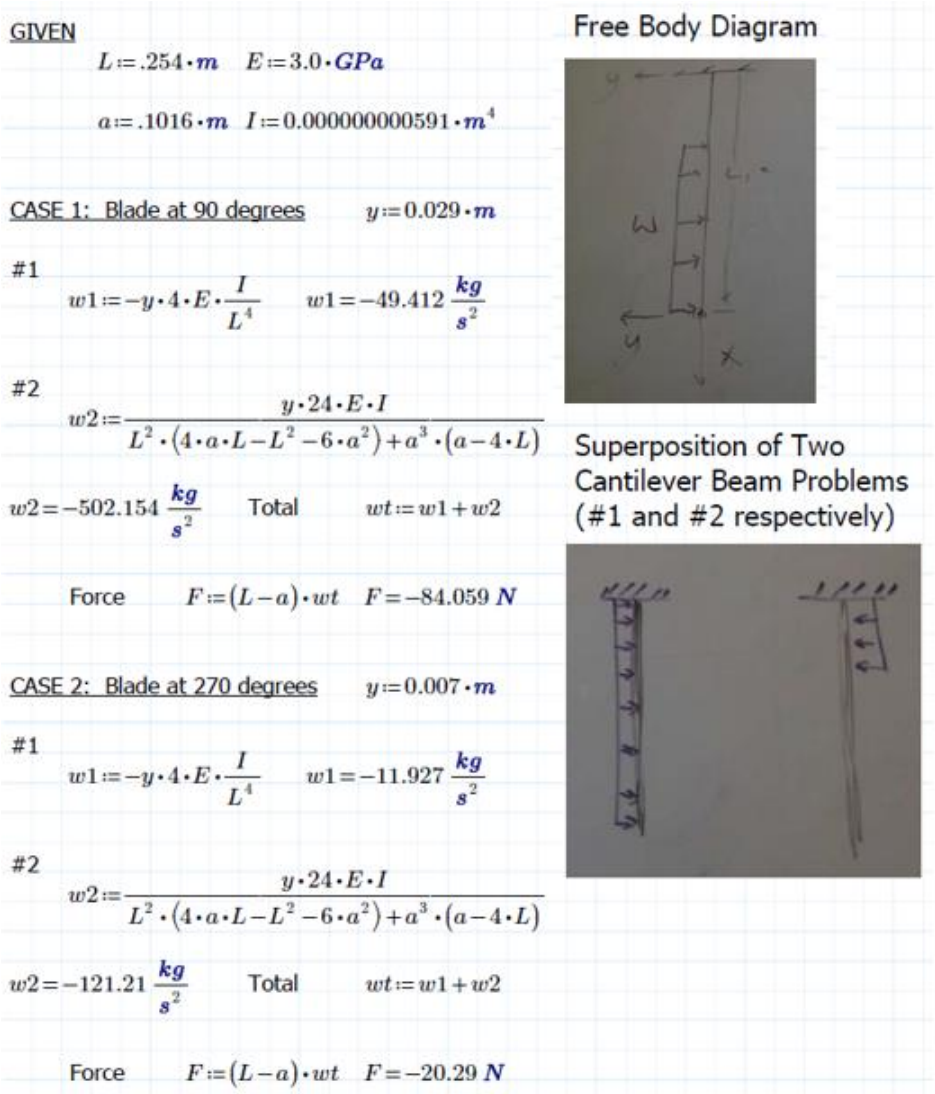

Figure B1: Calculation for estimated force of water on the blades